Chemical Geology 586 (2021) 120610

Contents lists available at ScienceDirect

Chemical Geology

journal homepage: www.elsevier.com/locate/chemgeo

Improving the reliability of Fe- and S-XANES measurements in silicate glasses: Correcting beam damage and identifying Fe-oxide nanolites in hydrous and anhydrous melt inclusions

Allan H. Lerner [a,*], Michelle J. Muth [a], Paul J. Wallace [a], Antonio Lanzirotti [b], Matthew Newville [b], Glenn A. Gaetani [c], Proteek Chowdhury [d], Rajdeep Dasgupta [e]

[a] Department of Earth Sciences, University of Oregon, OR 97403, USA
[b] Center for Advanced Radiation Sources, The University of Chicago, IL 60637, USA
[c] Department of Geology and Geophysics, Woods Hole Oceanographic Institution, Woods Hole, MA 02543, USA
[d] Department of Earth and Planetary Sciences, University of California, Riverside, CA 92521, USA
[e] Department of Earth, Environmental, and Planetary Sciences, Rice University, TX 77005, USA

ARTICLE INFO

Editor: Donald Dingwell

Keywords:
XANES
Beam damage
Nanolites
Sulfur
Iron
Melt inclusions

ABSTRACT

The redox state of silicate melts influences crystallization, element partitioning, and degassing behavior. Synchrotron-based micro-X-ray absorption near edge structure (μXANES) spectroscopy has emerged as a powerful tool for determining redox conditions through the direct measurement of speciation of multivalent elements such as iron and sulfur in silicate glasses. In particular, the high spatial resolution afforded by synchrotron μXANES makes it one of the few techniques available for determining redox conditions in melt inclusions, which can provide insights into pre-eruptive melt properties. However, the small size of melt inclusions, the deep penetration of X-rays, and irradiation-induced beam damage make μXANES measurements in melt inclusions challenging. Here we present data showing the rapid occurrence of Fe- and S-μXANES beam damage in experimental glasses, mid-ocean ridge basalt glasses, and olivine-hosted melt inclusions from the southern Cascade arc and Kīlauea Volcano and develop approaches to recognize and correct for beam damage through repeated rapid analyses. By applying a time-dependent correction to a series of rapid measurements (~82 s/scan) of Fe-μXANES pre-edge centroid positions, irradiation-induced photo-oxidation (Fe^{2+} to Fe^{3+}) can be corrected back to undamaged initial $Fe^{3+}/\Sigma Fe$ even in damage-susceptible hydrous glasses. Using this beam damage correction technique, hydrous basaltic melt inclusions from the southern Cascades have $Fe^{3+}/\Sigma Fe$ values that are ~0.036 lower (corresponding to -0.5 log units lower oxygen fugacity) than would have been indicated by standard Fe-μXANES measurements. Repeated, rapid analyses (150–300 s/scan) were also used to identify S-μXANES beam damage (photo-reduction of S^{6+} to S^{4+}), which was corrected with a peak fitting method to restore initial $S^{6+}/\Sigma S$. We observe that S-μXANES beam damage can occur rapidly even in low-H_2O mid-ocean ridge basaltic glasses and melt inclusions from Kīlauea Volcano, which are otherwise stable during even prolonged Fe-μXANES analyses. By mitigating and correcting for sulfur photo-reduction, we conclude that some mid-ocean ridge basaltic glasses contain 0.08–0.09 $S^{6+}/\Sigma S$, which is more sulfate than might be expected based on the reduced oxidation state of these glasses (near the fayalite-magnetite-quartz oxygen buffer). Using beam damage identification and correction techniques, the valence states of iron and sulfur can be accurately measured even in beam damage-susceptible glasses and melt inclusions. Finally, using Fe-μXANES, we demonstrate the presence of Fe-oxide nanolites within otherwise glassy, naturally quenched melt inclusions, which can complicate determination of iron valence state in affected glasses.

* Corresponding author at: 1272, University of Oregon, Eugene, OR 97403, USA.
E-mail address: lerner.allan@gmail.com (A.H. Lerner).

https://doi.org/10.1016/j.chemgeo.2021.120610
Received 29 January 2021; Received in revised form 15 September 2021; Accepted 28 October 2021
Available online 30 October 2021

1. Introduction

Synchrotron-based micro-X-ray absorption near edge structure (μXANES) spectroscopy has become a valuable petrologic tool for *in situ* determination of the valence state and molecular complexing of redox-sensitive elements in magmatic minerals and glasses (see review by Sutton et al., 2020). In particular, Fe- and S-μXANES have been applied to quenched volcanic glasses to advance our understanding of magmatic oxygen fugacity (fO_2) and complexing of species in glasses from Earth's mid-ocean ridges, hotspots, and volcanic arcs (Bonnin-Mosbah et al., 2001, 2002; Wilke et al., 2006; Berry et al., 2008; Kelley and Cottrell, 2009; Cottrell and Kelley, 2011; Brounce et al., 2014, 2017; Dyar et al., 2016; Lanzirotti et al., 2019; Moussallam et al., 2019; Sutton et al., 2020), as well as in igneous material from lunar and Martian samples (Righter et al., 2013; McCanta et al., 2017, 2019). The fO_2 of magmas exerts a major control on mineral stability and thereby the differentiation paths of magmas (Osborn, 1959; Kelley and Cottrell, 2012), including the behavior of important ore-forming species (e.g. Cr, Cu, Fe, Ti; Papike et al., 2016; Lanzirotti et al., 2019; Sutton et al., 2020). Additionally, fO_2 can significantly affect the solubility and degassing of multivalent volatiles (e.g., S, C) (Jugo, 2009; Jugo et al., 2010; de Moor et al., 2013; Jégo and Dasgupta, 2014; Moussallam et al., 2014, 2016; Helz et al., 2017; Head et al., 2018). A well-established approach to determining melt fO_2 is by measuring $Fe^{3+}/\Sigma Fe$ in quenched glasses (e.g., Kress and Carmichael, 1991; Borisov et al., 2018; O'Neill et al., 2018).

Iron occurs as both Fe^{2+} and Fe^{3+} in most terrestrial melts, and as Fe^{2+} or Fe^{0} in strongly reduced melts below the IW buffer (generally extraterrestrial) (Schreiber et al., 1987). Fe-XANES allows the mean valence state of iron in minerals and silicate glasses to be determined based on spectral features at energies below the iron absorption edge (pre-edge features), while higher energy features inform iron bonding coordination in minerals (e.g., Waychunas et al., 1983; Bajt et al., 1994; Wilke et al., 2001, 2004, 2006; Berry et al., 2003, 2008; Farges et al., 2004; Cottrell et al., 2009). Fe-XANES pre-edge features in glasses are specifically sensitive to valence state, and measured spectra can therefore be related to glass $Fe^{3+}/\Sigma Fe$ by comparison to suites of glass standards synthesized under controlled redox conditions and analyzed using Mössbauer spectroscopy (e.g., Berry et al., 2003; Wilke et al., 2004; Cottrell et al., 2009). Several published calibrations relate measured Fe-XANES spectral centroid position associated with Fe^{2+} and Fe^{3+} pre-edge peaks to $Fe^{3+}/\Sigma Fe$ in silicate glasses (Galoisy et al., 2001; Bonnin-Mosbah et al., 2001; Berry et al., 2003; Wilke et al., 2004, 2007; Cottrell et al., 2009; Dauphas et al., 2014; Zhang et al., 2016, 2018; Fiege et al., 2017). Other recent calibrations have used multivariate analysis of the entire Fe-XANES spectrum to determine iron valence in standard glasses measured by Mössbauer (Shorttle et al., 2015; Dyar et al., 2016).

Sulfur in silicate melts dominantly occurs as S^{2-} or S^{6+} (Carroll and Rutherford, 1988; Wilke et al., 2008). The transition between S^{2-} and S^{6+} species in silicate melts occurs over a relatively narrow fO_2 range near the Ni-NiO buffer (Carroll and Rutherford, 1988; Jugo et al., 2010; Botcharnikov et al., 2011), although there is evidence that this transition is dependent on temperature, pressure, and melt composition (Baker and Moretti, 2011; Klimm et al., 2012a; Fiege et al., 2014; Masotta and Keppler, 2015; Matjuschkin et al., 2016; Nash et al., 2019). S-XANES has been used to quantify the $S^{6+}/\Sigma S$ in glasses by fitting the relative intensity of absorption peaks for sulfide and sulfate species that occur at ~2475–2479 eV and ~2481–2483 eV, respectively (Paris et al., 2001; Métrich et al., 2002, 2009; Bonnin-Mosbah et al., 2002; Fleet et al., 2005; Jugo et al., 2010). These two sulfur species generally have distinct spectral absorbance features when present in silicate glasses. Based on melt composition and cooling history, reduced sulfur can also occur in a variety of metal-sulfide complexes, each of which has particular identifiable spectroscopic features (Li et al., 1995; Bonnin-Mosbah et al., 2002; Fleet et al., 2005; Head et al., 2018).

Fe- and S-XANES are particularly powerful techniques for investigating redox conditions of melt inclusions (MI), which are small parcels of quenched glass formed from melt entrapped within growing crystals. Melt inclusions are useful because they can preserve information on volatile concentrations and melt diversity that is otherwise lost during magma mixing, ascent, and eruption (Kent, 2008; Métrich and Wallace, 2008; Wallace et al., 2021). Melt inclusions in many systems of petrologic interest can be very small, with mean diameters of 10–100 μm. The small size of MI leaves μXANES (hereafter XANES) as one of the few techniques suitable for *in situ* measurements of element speciation (i.e., valence state and molecular coordination) within MI.

Inferring magma redox state from iron and sulfur valence in quenched glasses first and foremost requires accurate XANES measurements. The large penetrative depths of high-energy X-rays and oblique incident beam trajectories at many analytical facilities require careful sample preparation and analytical strategies to avoid signal contamination during Fe- and S-XANES measurements of MI and matrix glasses (Fig. 1). It has also been recognized that many glass compositions are susceptible to X-ray-induced changes in iron and sulfur speciation during analysis (i.e., beam damage) (Wilke et al., 2008; Métrich et al., 2009; Gonçalves et al., 2013; Moussallam et al., 2014, 2019; Cottrell et al., 2018; Blundy et al., 2020; Hughes et al., 2020). Although Fe-XANES measurements of nominally anhydrous basaltic and rhyolitic glasses are observed to be reproducible over a broad range of incident X-ray fluxes (Cottrell et al., 2009), hydrous volcanic glasses, particularly basaltic compositions, have been observed to undergo rapid oxidation of Fe^{2+} to Fe^{3+} with progressive irradiation (Cottrell et al., 2018; Moussallam et al., 2019). The exact mechanisms of iron photo-oxidation are not fully understood, but involve the production of photoelectrons and the local accumulation of charge in non-conductive materials, which alters the electron state of multivalent elements. The ensuing redox exchanges within glasses are accelerated by O-H volatilization or migration (Cottrell et al., 2018).

S-XANES measurements in silicate glasses have also been observed to undergo beam-induced changes in speciation, typically with S^{6+} being reduced to S^{4+} during progressive X-ray irradiation (Wilke et al., 2008; Métrich et al., 2009). Strategies to mitigate beam damage during Fe- and S-XANES measurements include reducing X-ray flux density (photon flux/analytical area) by using defocused beams, continually moving the sample during analysis, and/or decreasing incident photon flux (Wilke et al., 2008; Métrich et al., 2009; Klimm et al., 2012a; Brounce et al., 2017; Cottrell et al., 2018; Moussallam et al., 2019). Spatially resolved XANES beamlines are available at a number of synchrotron light sources worldwide with incident X-ray intensities ranging from 10^8 to 10^{12} photons/s (Sutton et al., 2020), where higher X-ray fluxes shorten analysis time by providing lower detection limits, but amplify beam damage concerns.

Many of these approaches to lessen beam damage are challenging to apply to MI owing to their small sizes. Smaller MI require more focused beam diameters to avoid contamination by the host mineral, but are thereby subject to higher photon densities and thus possible beam damage (e.g., Gaborieau et al., 2020; Tassara et al., 2020). Melt inclusions are often targeted for petrologic investigation specifically because they can retain magmatic volatiles that are otherwise lost from the external magma during ascent and degassing (Kent, 2008; Métrich and Wallace, 2008). However, silicate glasses with high H_2O contents have been observed to undergo larger changes in iron (and potentially sulfur) speciation during irradiation than what is observed in anhydrous silicate glasses (Cottrell et al., 2018; Moussallam et al., 2019). Hydrous MI may also be susceptible to the formation of nanolite crystals during quenching (Danyushevsky et al., 2002; Di Genova et al., 2018), which could lead to spurious interpretation of XANES spectra. These combined properties make it particularly challenging to apply XANES oxybarometry methods to the analysis of MI from volcanic arc environments, which tend to be both small and H_2O-rich.

To analyze these challenging MI, it is beneficial to develop XANES

approaches that both minimize changes in elemental speciation during irradiation and correct for changes that do occur. Applying generalized corrections to datasets is not ideal because differences in glass compositions and H_2O contents (e.g., caused by variable diffusive H^+ loss from MI before quenching) can lead to different MI susceptibilities to beam damage within the same deposit or even within the same host mineral.

In this study, we present techniques that aid in recognizing X-ray–induced changes in iron and sulfur valence in volcanic glasses and MI that result from XANES analysis. We then propose new time-dependent corrections for beam damage that does occur. For S-XANES, we also introduce a new spectral fitting approach that can account for the photo-reduction of S^{6+} to S^{4+} during analysis. Finally, we present a method to identify the presence of Fe-oxide nanolites in MI during Fe-XANES analysis. Collectively, these methods enable reliable quantification of iron and sulfur valence, and thereby melt redox state, from small and/or beam damage-susceptible glasses and MI.

1.1. XANES analysis of melt inclusions

1.1.1. Geometric considerations

At the Fe *K*-edge, the characteristic 1/e X-ray absorption depth in basaltic glass is ≈ 40 μm (Elam et al., 2002), and 120 μm ($1/e^3$) thick glass is therefore required for 95% absorption of X-rays during Fe-XANES measurements. X-ray absorption by Fe-bearing inclusions or crystalline host phases that may be present within the analytical path will be mixed with the signal of the targeted glass. This is a particular problem for analyzing MI, as MI are often less than 100 μm thick. Consequently, most MI must be doubly intersected for Fe-XANES analysis to avoid signal contamination from the host mineral. A further complication in XANES measurements of MI, particularly for highly penetrative Fe-XANES analyses, is that many μXANES beamline configurations utilize a ~45° slant geometry of incoming X-ray beam in fluorescence operating modes. The inclined incidence angle means that as wafer thickness increases in the beam direction, progressively wider doubly-intersected MI areas are needed to keep the analytical path free of mineral contamination (Fig. 1). Throughout the X-ray penetration volume, the minimum required doubly-intersected MI dimensions for a host-free glass measurement are equal to the MI thickness plus the beam diameter size (assuming a cylindrical doubly-intersected MI area). This requires MI to be either sufficiently wide or ground very thin for clean glass analyses using high energy X-rays (e.g., Fe-XANES, V-XANES, Cu-XANES). Thus, small MI in olivine and other Fe-bearing phases can be challenging to measure for Fe-XANES. Even for analyses of MI in phases that have low, but non-zero, Fe-concentrations (e.g., feldspars), the high penetrative depth of Fe-XANES can excite a large volume of the host phase, so that the host contribution to the Fe-XANES signal may be significant. This issue is of particular concern for small MI and for glass compositions with relatively low Fe-contents, such as dacites and rhyolites. At the lower energy S *K*-edge (~2500 eV), X-rays are more strongly attenuated, with the 1/e X-ray absorption depth in basaltic glass only ~5 μm. Consequently, 95% of the S-XANES X-ray absorption occurs within the upper 15 μm Wilke et al. (2011), and most of these geometric concerns are accordingly lessened (Fig. 1A).

1.1.2. Analytical details and sample descriptions

Fe- and S-XANES measurements were conducted on a variety of volcanic and experimental silicate glasses at GSECARS beamline 13-ID-E at Argonne National Laboratory's (Illinois, USA) Advanced Photon Source (APS), a third generation synchrotron light source (Sutton et al., 2017). Details of the 13-ID-E beamline configuration are described in Head et al. (2018) and are consistent with measurements conducted here, except for differences in photon flux and analytical times described below.

To account for differences in monochromator calibrations between synchrotron facilities, a set of standards (minerals, metal foils, synthetic glasses) were measured at the onset of each analytical session to determine the appropriate energy offset to apply to Fe- and S-XANES oxybarometer calibration curves relative to reference energy fitting ranges (details below). At beamline 13-ID-E, the lattice constants for the monochromator Si(111) and Si(311) crystals are calculated from reference foils measured throughout the analyzable energy range of the crystals, and provide excellent consistency with absorption edge

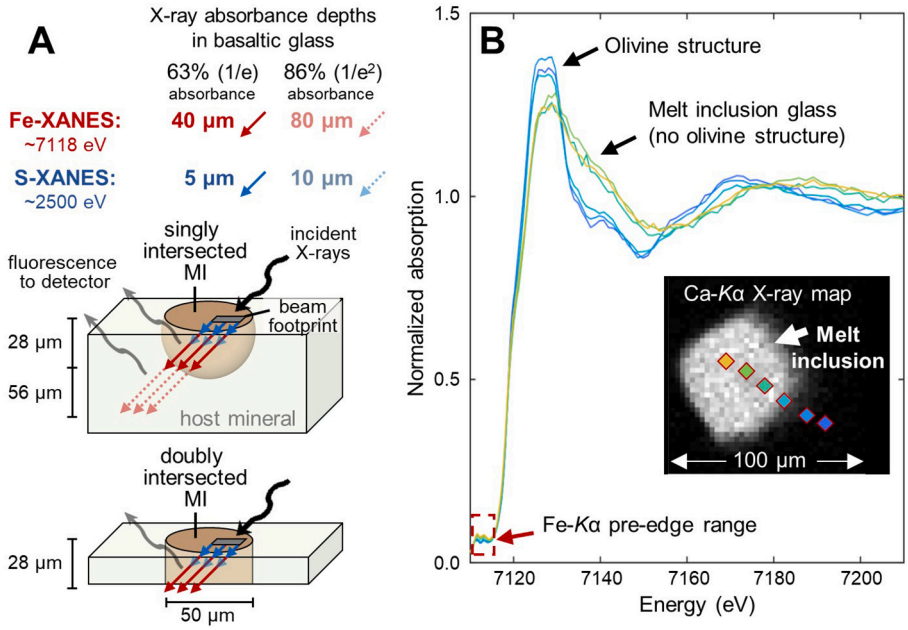

Fig. 1. *(A)* Schematic analytical XANES geometry of a 50 μm diameter melt inclusion (MI) (brown) analyzed with a 20 × 20 μm X-ray beam. For many XANES fluorescence measurements, the X-ray beam (black arrow) is ~45° incident to the sample surface and the sample fluorescent energy (gray arrows) is measured at 45° in the opposite direction. Depending on the penetration depth of the X-ray energy being used, the beam may interact with substantial host mineral both laterally and at depth, leading to mineral-contaminated spectra. For Fe-XANES (red arrows), 63% and 86% of the X-ray signal are absorbed in 40 and 80 μm hypotenuse paths through basaltic glass (28 and 56 μm vertical thicknesses), requiring the MI be both doubly intersected and sufficiently wide to avoid host mineral contamination. S-XANES X-ray energies are much less penetrating (blue arrows), so MI geometry and thickness concerns are lessened. *(B)* A series of Fe-XANES measurements of a doubly-intersected olivine-hosted MI from the southern Cascades (BORG-1_37, Table 1) showing a traverse from within the MI into the olivine-host, demonstrating the difference in absorption edge profiles of glass and olivine analyses. Measurement locations are shown atop a Ca-*K*α X-ray map (inset), with symbol colors matching the shown spectra. (For interpretation of the references to color in this figure legend, the reader is referred to the web version of this article.)

energies determined by Kraft et al. (1996). The 13-ID-E beamline has excellent reproducibility in measured reference materials over the course of standard two to three-day measurement periods and therefore no within-session drift corrections were applied during either Fe- or S-XANES measurements. Prior to each XANES analysis, an X-ray map was made by rapidly rastering across the sample to identify areas in MI and other glass targets that were free of host mineral or microlite crystals in the beam path. The X-ray beam was then turned off to prevent any further unnecessary beam interaction with the glasses until XANES measurements began.

Analyzed samples include doubly-intersected MI and matrix glasses mounted on Fe-free glass rounds and thin sections. Samples were embedded in CrystalBond®, EpoThin® epoxy, or thin section resin. All bonding material and glass substrates were analyzed to confirm that they contained only trace amounts of iron and had negligible contribution to Fe-XANES signals. The bonding materials did contain substantial sulfur, but because the lower energy X-rays for S-XANES are almost fully absorbed within ~15 μm of glass (Fig. 1A) and all analyzed glasses were substantially thicker than this, the bonding materials contributed no appreciable signal to S-XANES measurements. We also analyzed singly intersected experimental glass charges, where glass thicknesses of multiple mm fully absorbed X-rays at both Fe- and S-*K*α energies so that contamination from the capsule material was insignificant. In experimental glass charges, care was taken to analyze only crystal-poor glass areas and to avoid measurements near capsule edges.

2. Identifying and correcting Fe-XANES beam damage

Fe-XANES measurements were made in fluorescence mode at APS during analysis sessions in 2018 and 2019. The APS 13-ID-E beamline can deliver a focused, unattenuated X-ray beam to the sample at the Fe *K*-edge energy with photon fluxes exceeding 1×10^{12} photons/s. Fully focused beam sizes of ~1×2 μm are achievable, providing flux densities up to 5×10^{11} photons/s/μm^2. Cottrell et al. (2018) and Moussallam et al. (2019) show that beam damage during Fe-XANES analysis scales with delivered photon dose over the measurement duration. Therefore, for the analyses presented here, photon doses were reduced during Fe-XANES analyses as follows:

1) Photon flux was attenuated using high-purity aluminum foil filters in the beam path (6 sheets of foil, totaling 222 μm thick), which decreased the incident photon flux to ~3–5 $\times$ 10^9 photons/s, consistent with an approach used in previous studies (Brounce et al., 2017; Moussallam et al., 2019; Tassara et al., 2020; Gaborieau et al., 2020).
2) Flux density on the sample was further decreased by defocusing the incident X-ray beam so that photon densities were generally 1–1.5 $\times$ 10^8, 2–4 $\times$ 10^7, and 6–9 $\times$ 10^6 photons/s/μm^2 for 5×5, 10×10, and 20×20 μm beam footprints, respectively.
3) Analysis times were minimized as much as possible while still providing interpretable spectra, which allowed us to reduce beam exposure.

The 13-ID-E monochromator calibration provides a first derivative of the Fe *K*-edge peak of iron foil at ~7110.7 eV, consistent with values determined by Kraft et al. (1996). We followed the Fe-XANES measurement methodology outlined in Head et al. (2018), but with modified scan times and energy ranges used to better identify and correct for beam damage. Two different analytical setups were used: rapid pre-edge scans and slower full energy scans. For rapid scans, the incident beam was scanned from 7092 to 7107 eV in 2.5 eV steps, from 7107 to 7119 eV in 0.1 eV steps, and from 7119 to 7144 eV in 0.05 Å^{-1} (0.5–1.0 eV) steps (continuous steps rather than discrete). Each scan step was 0.5 s and the total scan time was 82 s, with ~10 s delay prior to the next analysis for beamline adjustment and computational processing. The rapid pre-edge scans quickly measure over a reduced energy range to minimize beam exposure to the extent possible while still collecting spectra with high enough resolution for peak fitting in the pre-edge region. The 82 s scan is much faster than typical Fe-XANES scan durations reported in the literature, which usually range from 270 s to >700 s (4.5 to >10 min) (e.g., Cottrell et al., 2009, 2018; Moussallam et al., 2016; Head et al., 2018; Gaborieau et al., 2020; Tassara et al., 2020). The slower, full energy range scans measured from 7012 to 7102 eV in 2.5 eV steps, from 7102 to 7120 eV in 0.1 eV steps, and from 7120 to 7356 eV in 0.05 Å^{-1} (0.5–3.0 eV) steps. Each scan step time was either 0.5 or 1 s and total scan durations were 176 or 352 s. This full energy range scan served as a higher-resolution scan of both the pre- and post-absorption edge regions, which is similar to analytical procedures reported in other Fe-XANES studies and allowed spectra to be normalized and assessed for mineral contamination.

Measured spectra were normalized to the incident flux (*K*α fluorescent intensity / incident flux [I0]) and were fit using XAS viewer within the LARCH software package (Newville, 2013). $Fe^{3+}/\Sigma Fe$ was calculated using relative pre-edge peak intensities following approaches described in Cottrell et al. (2009). This approach uses the calculated centroid energy of the pre-edge doublet, which is related to the 1s → 3d electron transition, to determine glass $Fe^{3+}/\Sigma Fe$ based on calibrations to standard glasses equilibrated at known fO_2 conditions and measured using Mössbauer spectroscopy (Berry et al., 2003; Wilke et al., 2004; Cottrell et al., 2009). An energy offset between our basaltic glass measurements and those used in the Fe-XANES calibration of Cottrell et al. (2009) (due to monochromator calibrations and background subtractions during peak fitting) was determined by comparing the Fe pre-edge centroid position of basaltic reference glass LW_0 (Cottrell et al., 2009, 2018; Zhang et al., 2016, 2018) from the Smithsonian Institution. The split of LW_0 glass analyzed here is embedded in the mount NMNH 118279/IGSN NHB007V34, and is the same specimen as found in the mount with catalog number NMNH 117393/IGSN NHB0073V8 (both available by request from the Smithsonian Institution). The pre-edge centroid position of LW_0 was measured by Cottrell et al. (2009) to have an energy of 7112.30 eV using the beamline configuration they described at the National Synchrotron Light Source (Brookhaven National Laboratory). All Fe-XANES spectra in figures and data tables throughout this manuscript are presented in energy units as-measured at APS. However, when calculating iron valences in basaltic glasses, energy shifts of +0.317 and + 0.323 eV were respectively applied to iron pre-edge centroid positions for measurement sessions 2018–3 and 2019–2 to provide consistency with centroid values measured for LW_0 in Cottrell et al. (2009). Pre-edge peak fitting ranges were similarly adjusted from Cottrell et al. (2009) to span an energy range of 7108.7–7116.7 eV, consistent with the methodology discussed in Zhang et al. (2016). Within this fit window, the absorption baseline of the main Fe *K* absorption edge was fit using a linear and a Lorentzian function, and the pre-edge doublet was fit using two Gaussian functions (Cottrell et al., 2009). The centroid value of the these two peaks was used to calculate $Fe^{3+}/\Sigma Fe$ following the Mössbauer-based calibration of Zhang et al. (2018) for basaltic glasses.

For dacitic and rhyolitic glasses, average iron valence was calculated from a parameterization of Fiege et al. (2017) for felsic glasses. No energy offsets were applied because our measurements of the first derivative of the absorption edge of iron foil were consistent with those of Fiege et al. (2017). Uncertainties in centroid values (±1 SE), as detailed below, are propagated through the basalt or rhyolitic calibrations to calculate uncertainties of $Fe^{3+}/\Sigma Fe$ calculations.

2.1. Timescales of Fe-XANES beam damage

Fe-XANES analysis of hydrous silicate glasses with a high intensity X-ray beam can cause rapid photo-oxidation of Fe^{2+} to Fe^{3+} within the glass, creating large inaccuracies in determining the initial $Fe^{3+}/\Sigma Fe$ values of glasses (Cottrell et al., 2018; Moussallam et al., 2019) (Fig. 2). The extent of this oxidation varies depending on glass composition and photon dose. Beam-induced oxidation causes a shift in Fe-*K*α pre-edge

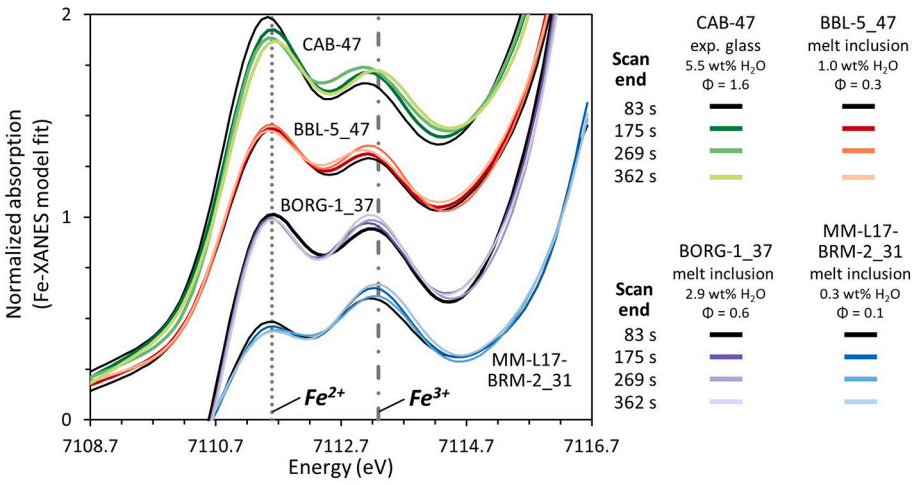

Fig. 2. Model fits to Fe-XANES pre-edge spectra for repeated rapid scans of experimental basaltic glass CAB-47 and of melt inclusions from the southern Cascades (CA, USA). Spectra of different samples have been vertically shifted for clarity. Progressive oxidation occurs during repeated rapid scans, as evidenced by the lighter colored lines. Samples have different initial $Fe^{3+}/\Sigma Fe$ and H_2O contents, which affect the extent of beam-induced photo-oxidation. Measurements were made with a 10 × 10 μm beam and photon flux densities ranging from 2 to 4 × 10^7 photons/s/μm^2. The lines labeled Fe^{2+} and Fe^{3+} refer to the approximate positions of the first and second pre-edge doublet peaks.

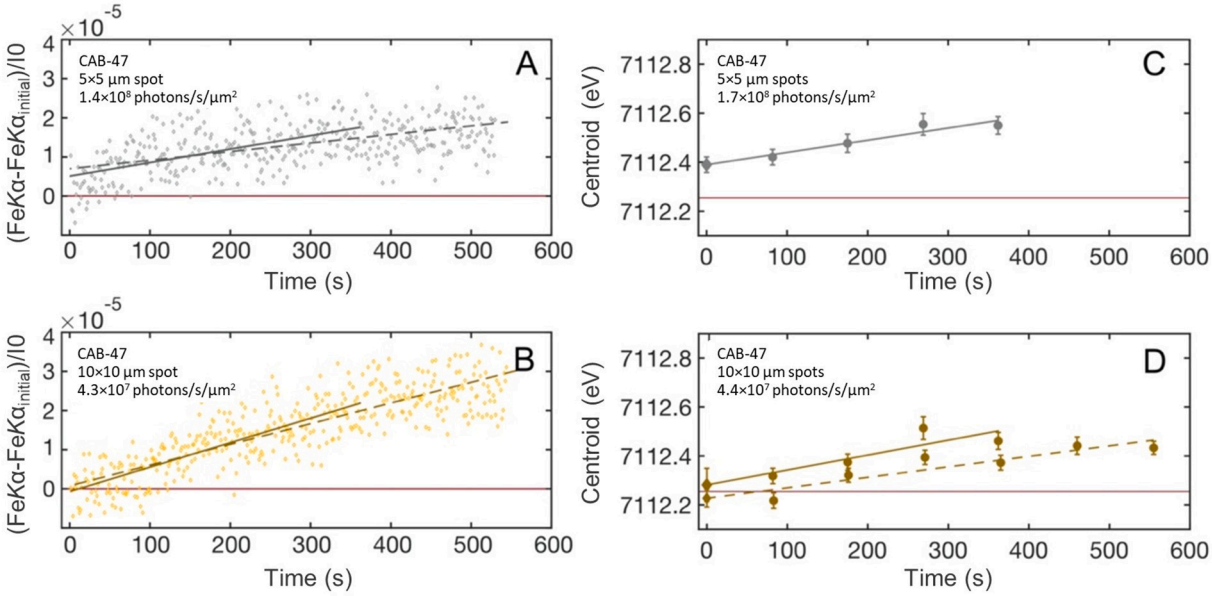

Fig. 3. *(A, B)* Intensities of the 2nd pre-edge doublet as a function of time in experimental glass CAB-47 measured with photon flux densities of 1.4 × 10^8 and 4.3 × 10^7 photons/s/μm^2 (5 × 5 μm and 10 × 10 μm respective spot sizes). Gray and yellow lines are linear regressions through data from 0 to 362 s (solid) or 0 to 537 s (dashed). Fe-*K*α/I0 initial intensity (red horizontal line) is taken as the average of the first 5 analyses. *(C, D)* Pre-edge centroid positions calculated from repeated rapid scans (see Fig. 2) for experimental glass CAB-47 with photon flux densities of 1.7 × 10^8 photons/s/μm^2 (5 × 5 μm spot size; one time series) and ~4.4 × 10^7 photons/s/μm^2 (10 × 10 μm spot size, two time series). Each circle is a centroid value calculated from one pre-edge scan with error bars representing ±1 SE of centroid fits to each scan. Diamonds at $t = 0$ s are the intercept of linear regressions to each time series and are taken to be beam damage-corrected centroid values. Error bars on the t = 0 s centroid positions represent ±1 SE of the time series linear regression. Red lines in panels *C* and *D* are the estimated initial t = 0 s centroid value, which is taken as the average beam damage corrected centroid values for the two 10 × 10 μm analysis time series (panel *D*). Gray and yellow lines are linear regressions through centroid values from 82 to 362 s (solid) and 82 to 537 s (dashed). Centroid values in *C* and *D* have been shifted by +0.32 eV for consistency with the LW_0 centroid position reported by Cottrell et al. (2009).

peak intensities but does not produce any uniquely identifiable spectral features. Consequently, it is impossible to know from a single Fe-XANES analysis whether a sample had suffered from beam-induced photo-oxidation (compare with S-XANES beam damage, which produces diagnostic spectral features, as discussed below). Therefore, samples must either be analyzed under carefully tested analytical conditions to ensure that no significant beam damage occurs for the particular glass composition and analysis duration, or a method must be employed that can identify and correct for beam damage in each individual analysis spot. We emphasize the latter approach in this study, presenting a method that allows us to reliably analyze small, hydrous glass inclusions with a relatively high-flux beam.

To identify and correct for beam damage within each analysis spot, we conducted multiple rapid scans of the Fe *K* pre-edge region to create a time series of progressive photo-oxidation (Fig. 2). These time series allow us to assess whether beam damage occurred during analysis and, if needed, enables us to calculate sample-specific corrections. For each analysis spot, we conducted 3 to 6 rapid pre-edge scans (82 s) followed by one full energy scan (176 or 352 s) across the entire Fe *K* absorption edge energy range. If pre-edge centroids calculated from the rapid scans did not show progressive oxidation over time, the spectra were merged together to form a single higher-resolution pre-edge spectrum. If progressive changes in pre-edge centroid positions were observed, we use the time series of centroid positions to extrapolate the centroid back to *t*

Table 1
Experimental and natural glasses analyzed by Fe- and S-XANES in this study.

Sample, composition	H_2O (wt %)	Fe-XANES beam damage susceptibility index (Φ)*	XANES analysis type	$Fe^{3+}/\Sigma Fe$ and $S^{6+}/\Sigma S$ ranges**	Photon density (photons/s/μm^2); observed beam damage***
CAB-47: experimental basaltic glass. 1250 °C, 1.3 GPa, minor phenocrysts (Weaver et al., 2011; this study)	5.5	1.6	Fe-XANES (+ photo-oxidation time series tests) S concentration too low for S-XANES	0.13 Fe^{3+}	Fe-XANES: 1–1.5 × 10^8: high 2–4 × 10^7: high 6–9 × 10^6: med
CAB-33: experimental basaltic glass. 1225 °C, 1.7 GPa, phenocryst-free, but Fe-oxide nanolite spectral signature (Weaver et al., 2011; this study)	7.2	1.8	Fe-XANES (+ photo-oxidation time series tests) S concentration too low for S-XANES	Fe-oxide nanolites present	Fe-XANES: 2–4 × 10^7: severe 6–9 × 10^6: high
P2-F: Mono Craters obsidian pyroclast with <0.1% microlites (Barnes et al., 2014; Watkins et al., 2017; this study)	2.0–2.3	–	Fe photo-oxidation time series tests	–	Fe-XANES: 1–1.5 × 10^8: med 2–4 × 10^7: slight
G466: experimental basalt glass. 1300 °C, 2 GPa, minor clinopyroxene + anhydrite (Chowdhury and Dasgupta, 2019; this study)	6.5	–	S-XANES	1.0 S^{6+}	S-XANES: 5 × 10^9: severe 2 × 10^8: high 5 × 10^7: med 8 × 10^6: slight
G479: experimental basalt glass. 1300 °C, 1.5 GPa, minor anhydrite (Chowdhury and Dasgupta, 2019; this study)	8.9	–	S-XANES	1.0 S^{6+}	S-XANES: 8 × 10^6: slight
MORB glasses: VG-2 (Jarosewich et al., 1980; Rose and Brown, 2017; Zhang et al., 2018; this study) JDF-46 N (Fiege et al., 2014; this study) ALV892–1 (Fiege et al., 2014; this study)	<0.1	~0.01	S-XANES	~0.15 Fe^{3+} 0.04–0.08 S^{6+}	S-XANES: 1 × 10^{10}: severe 4.5 × 10^8: high 1 × 10^8: med 6.5 × 10^6: slight
KE62-3293S: Kīlauea 2018 basaltic pumice MI and matrix glass (Lerner et al., 2021; this study)	0.1–0.3	0.1	Fe-XANES S-XANES	0.13–0.18 Fe^{3+} 0.03–0.25 S^{6+}	Fe-XANES: 2–4 × 10^7: none S-XANES: 2 × 10^8: med 5 × 10^7: slight 8 × 10^6: none
KE62-3315F: Kīlauea 2018 littoral bomb MI and matrix glass (Lerner et al., 2021; this study)	0.1–0.2	0.03	Fe-XANES S-XANES	0.20–0.34 Fe^{3+} 0.68–0.96 S^{6+}	Fe-XANES: 2–4 × 10^7: none S-XANES: 5 × 10^7: high 8 × 10^6: slight
Lassen (southern Cascades): olivine-hosted MI BRM, BBL, BORG (Muth and Wallace, 2021; this study)	0.3–3.7	0.1–0.7	Fe-XANES S-XANES	0.14–0.31 Fe^{3+} 0.20–0.98 S^{6+}	Fe-XANES: 2–4 × 10^7: med S-XANES: 5 × 10^7: med 8 × 10^6: slight
Augustine 2006: AUG_308 – low silica andesite tephra; AUG_HSA2 – high silica andesite tephra (Lerner, 2020; this study)	1.0–4.0	0.2	Fe-XANES	0.39–0.44 Fe^{3+} (in glasses with no Fe-oxide nanolites)	Fe-XANES: 1–1.5 × 10^8: slight to none
Cerro Negro: olivine-hosted MI (Gaetani et al., 2012; this study)	3.0–4.0	0.5	Fe-XANES	Fe-oxide nanolites present	Fe-XANES: not tracked with repeat scans

* Fe-XANES beam damage susceptibility index (Cottrell et al., 2018): $XHO_{0.5}$ * $XFeO/XFeO_{1.5}$, calculated using molar fractions and Fe^{2+}/Fe^{3+} from time-zero interpolated Fe-XANES measurements. Full glass compositions are presented in the Data supplement.

** $Fe^{3+}/\Sigma Fe$ and $S^{6+}/\Sigma S$ ranges for beam damage corrected Fe- and S-XANES analyses. XANES spectra and results are presented in the Data supplement.

*** Incident photon flux was ~3–5 × 10^9 photons/s for Fe-XANES, and ~1–50 × 10^9 photons/s for S-XANES. Analysis footprint sizes ranged from 2 × 2, 5 × 5, 10 × 10, 20 × 20, and 50 × 50 μm. Qualitative beam damage observations were based on 2–4 repeated scans, with total scan times of 8–12 min and 10–15 min per location for Fe- and S-XANES measurements, respectively.

= 0 s. We take this extrapolated value as the initial, 'correct' centroid position prior to beam exposure. This time-dependent correction approach is similar to methods commonly applied to electron microprobe (EPMA) measurements to account for alkali migration during electron beam excitement (Kuehn et al., 2011). A time-dependent approach has also been recently proposed for determining iron valence by EPMA measurements (Hughes et al., 2018).

X-ray-induced photo-oxidation during Fe-XANES analysis can be difficult to identify, partly because a large extent of the valence change occurs rapidly in the first minutes of analysis (Cottrell et al., 2018; Moussallam et al., 2019). To ensure that our sequences of repeated rapid scans adequately captured changes to centroid positions during the earliest stages of photo-oxidation, we measured changes to the intensity of the 2nd pre-edge doublet (7113.2–7113.4 eV at APS) in single spots over 6–16 min. Such dwell tests track the photo-oxidation of the analyzed glass at a much finer temporal resolution than pre-edge scans allow (Shorttle et al., 2015; Cottrell et al., 2018; Moussallam et al., 2019; Gaborieau et al., 2020). However, one limitation to such single-energy dwell tests are that other simultaneously changing spectral features cannot be detected. Additionally, one must assume that any changes in spectral background during the measurement duration are negligible.

We conducted a set of dwell tests on an experimental basaltic glass (CAB-47, Weaver et al., 2011) (Fig. 3A, B) with a high H_2O content (5.5 wt%) and a high proportion of Fe^{2+} (~0.13 $Fe^{3+}/\Sigma Fe$). Sample CAB-47 shows larger degrees of beam-induced iron oxidation compared to the natural glasses studied here, likely due to its combined high H_2O and Fe^{2+} contents (Cottrell et al., 2018). The calculated beam damage susceptibility index (Φ, where $\Phi = XHO_{0.5}$ * $XFeO/XFeO_{1.5}$), as described in

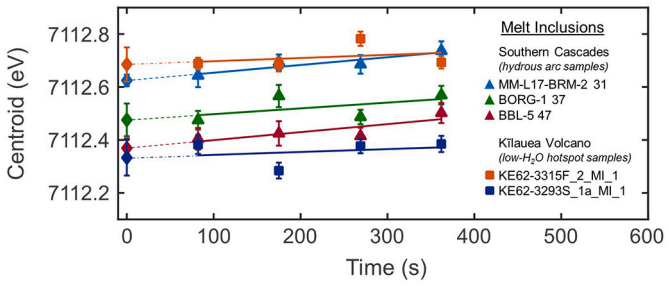

Fig. 4. Fe-*K*α pre-edge centroid positions calculated from repeated rapid scans of MI from the southern Cascades (triangles) and from Kīlauea Volcano (squares). Symbols are the centroid values calculated from individual pre-edge scans and error bars represent ±1 SE for each centroid fit. Lines are linear regressions through centroid values from 82 to 362 s. Diamonds at t = 0 s are the intercept of each regression (dashed lines), taken to be the beam damage-corrected centroid positions. Error bars on diamonds represent ±1 SE of the time series linear regression. Analyses used a 10 × 10 μm spot size, which resulted in photon flux densities of 3–5 × 10^7 photons/s/μm^2. All centroids have been shifted by +0.32 eV for consistency with the LW_0 centroid position reported by Cottrell et al. (2009). Hydrous MI from the southern Cascades underwent progressive photo-oxidation, whereas less damage-susceptible MI from Kīlauea Volcano remained stable.

Cottrell et al. (2018), is 1.6 for CAB-47 compared to Φ of 0.1–0.7 for the various natural MI investigated in this study (Fig. 5, Table 1). We therefore use this highly beam damage-susceptible experimental glass to evaluate models for correcting changing iron valence during Fe-XANES analysis.

To evaluate if time series of repeated rapid pre-edge scans (82 s durations, described above) are sufficiently fast to capture photo-oxidation in CAB-47, we compared the pre-edge rapid scan time series to the 2nd pre-edge doublet dwell tests in the same glass (Fig. 3, Fig. A.1). It is assumed that the rate of change of the 2nd pre-edge doublet intensity scales with the change in centroid value during time series analyses (Cottrell et al., 2018; Moussallam et al., 2019). Dwell tests of the 2nd pre-edge doublet of CAB-47 with a photon flux density of ~1.4 × 10^8 photons/s/μm^2 (analyzed with a 5 × 5 μm spot size) show that substantial photo-oxidation occurs in the first minute of analysis, with $Fe^{3+}/\Sigma Fe$ increasing from 0.13 to 0.19. Under these high photon flux densities, photo-oxidation progresses non-linearly (Cottrell et al., 2018; Moussallam et al., 2019; Fig. 3, Fig. A.1). The time series of repeated rapid pre-edge scans cannot capture this non-linear behavior that occurs in the initial 10s of seconds of analysis, and therefore cannot adequately characterize photo-oxidation at such high photon flux densities (Fig. 3A, C). However, by decreasing the photon flux density to ~4.3 × 10^7 photons/s/μm^2 (using a 10 × 10 μm spot size), dwell tests of CAB-47 show that photo-oxidation progresses slowly enough that changes to both the 2nd pre-edge doublet intensity and centroid values can be adequately approximated by fitting a linear function to repeated rapid pre-edge scans (Fig. 3B, D). Although photo-oxidation may remain non-linear in the initial minute of analysis even at this lower photon dose, the linear fit approximates the data within typical measurement uncertainty and is thus a reasonable approximation. The progression of photo-oxidation becomes more linear with further decreased photon flux densities (Fig. A.1).

The same dwell tests were conducted using similar photon densities on another experimental hydrous basaltic glass (CAB-33, 7.2 wt% H_2O, Φ = 1.8; Weaver et al., 2011) and on a moderately hydrous natural obsidian pyroclast from Mono-Inyo Craters (CA, USA) (P2-F, ~2.2 wt% H_2O; Barnes et al., 2014; Watkins et al., 2017; Table 1). Observed changes to the 2nd pre-edge doublet intensity in these glasses were similar to those measured in CAB-47 (Fig. A.1), suggesting that the time series correction approach can be applied across a range of basalt to rhyolite glass compositions, including hydrous samples that are highly susceptible to photo-oxidation.

2.2. *Applying the Fe-XANES beam damage correction technique to natural melt inclusions*

Because glass CAB-47 is more susceptible to beam damage than most MI and matrix glasses, changes to Fe-*K* pre-edge centroids in most natural samples analyzed under the same conditions (~3.0 × 10^7 photons/s/μm^2) can also be approximated with a linear function. Hydrous basaltic MI from the southern Cascades arc (0.3–3.7 wt% H_2O, Φ = 0.1–0.7) show consistent increases in pre-edge centroid values over the course of several repeated rapid scans, indicating progressive photo-oxidation (Fig. 4, Table 1). In contrast, basaltic MI from Kīlauea Volcano (HI, USA) do not show time-dependent changes to pre-edge centroid values, as expected based on their low H_2O contents and low beam damage susceptibilities (0.1–0.3 wt% H_2O, Φ ≤0.1) (Fig. 4, Table 1). The slopes of linear regressions to pre-edge centroid time series (i.e., the rate of photo-oxidation) are inversely correlated with calculated initial $Fe^{3+}/\Sigma Fe$ and are positively correlated with H_2O contents of glasses (Fig. 5, Fig. A.2). These observations are consistent with beam damage occuring more readily in reduced and/or hydrous glasses (Blundy et al., 2020; Cottrell et al., 2018).

To apply time series corrections in beam damage-susceptible samples, linear regressions using 4 rapid pre-edge scans are generally sufficient to correct to initial (t = 0 s) centroid positions. However, using up

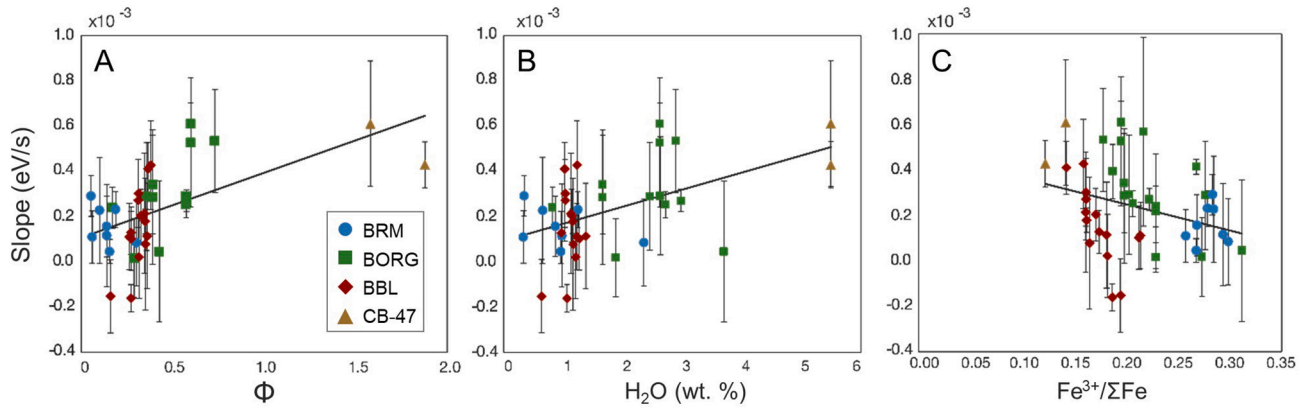

Fig. 5. Slopes of linear regressions through Fe-*K* pre-edge centroid value time series for individual glasses plotted as a function of *(A)* beam damage susceptibility index (Φ = $XHO_{0.5}$ * $XFeO/FeO_{1.5}$) as defined in Cottrell et al. (2018), *(B)* H_2O content, and *(C)* initial $Fe^{3+}/\Sigma Fe$. Melt inclusions from southern Cascades cinder cones (BORG, BRM, BBL) and experimental glass analyses (CAB-47) are grouped by color. Gray lines are linear regressions through analysis spots from all natural and experimental samples.

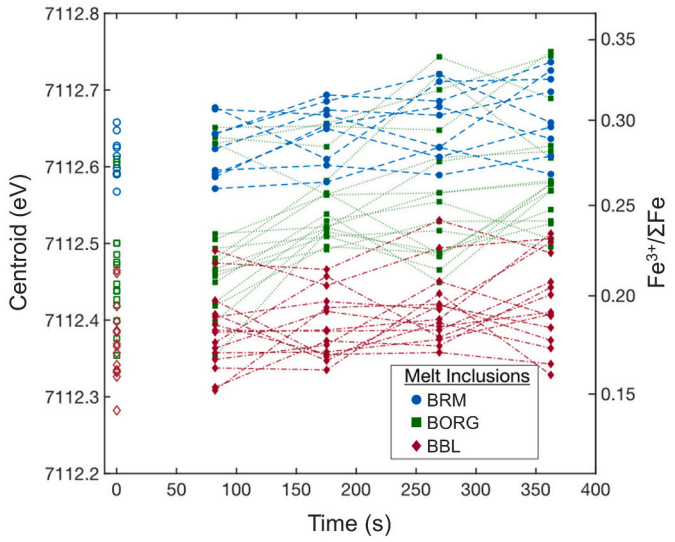

Fig. 6. Fe-*K*α pre-edge centroid positions through time calculated from repeated pre-edge scans for individual southern Cascades MI. Dashed lines connect centroids calculated from four consecutive rapid scans of the same analysis spot, and open symbols at t = 0 s are the corrected initial centroids. Centroid time series measurements are plotted at the end time of each scan. Right vertical axis is the calculated $Fe^{3+}/\Sigma Fe$ from centroid values using the calibration of Zhang et al. (2018). All centroids have been shifted by +0.32 eV for consistency with the LW_0 centroid position reported by Cottrell et al. (2009).

to 6 pre-edge scans can provide an improved regression fit, as increased scans minimize the leverage of anomalously noisy analyses in the regression (Fig. 3D). Uncertainties in restored initial centroid positions were assessed by *A)* calculating the standard error of regression for each time series and by *B)* calculating the standard deviation of time series linear fits using a Monte Carlo method that incorporates the standard error of each individual centroid fit (Browaeys, 2021). For the analytical conditions used in this study, these two approaches yield similar uncertainty estimates for the t = 0 s centroid positions (Fig. A.3). Weighting the linear regressions by the inverse of the squared standard deviation of each measurement's uncertainty also yields similar linear fits and standard error estimates for t = 0 s centroid values. In time series with substantial scatter in centroid positions, the standard error of linear regressions is generally larger than the Monte Carlo-derived uncertainty estimates (Fig. A.3). We therefore use the standard error of unweighted linear regressions to estimate uncertainties in the restored t = 0 s centroid positions, as this is the simplest and generally most conservative approach.

For hydrous basaltic MI from the southern Cascades, the average 1 standard error of regression for corrected t = 0 s centroid values is ±0.04 eV, or ± 0.02 $Fe^{3+}/\Sigma Fe$ when propagated through the calibration of Zhang et al. (2018) (note that curvature of the calibration function increases $Fe^{3+}/\Sigma Fe$ uncertainties in more oxidized glasses). This uncertainty is only slightly larger than the average standard error of centroid value fits of our higher resolution full length scans (±0.03 eV; ±0.01 $Fe^{3+}/\Sigma Fe$), and is much smaller than the ~0.15 variation in $Fe^{3+}/\Sigma Fe$ measured in basaltic arc MI globally (Kelley and Cottrell, 2009; Brounce et al., 2014; Muth and Wallace, 2021). Regressions on replicate analyses within the same MI yield corrected t = 0 s centroid positions that are within error of each other (Fig. A.4), indicating that this beam damage correction approach is reasonably accurate.

2.3. Discussion and summary

Although the time-dependent beam damage correction approach introduces some imprecision, it ensures that data sets are not systematically biased to higher calculated $Fe^{3+}/\Sigma Fe$ values due to uncorrected photo-oxidation. In analyses of basaltic MI from the southern Cascades (measured with photon flux densities of 1–5 × 10^7 photons/μm/s^2), the difference between corrected and uncorrected centroid positions is large (Fig. 6). On average, Fe-*K* pre-edge centroid values measured after 362 s of analysis are 0.09 eV higher than *t* = 0 s corrected centroid values. This means that despite measures taken to lower the photon flux, had we analyzed these hydrous MI with more typical 10 min duration scans (where the pre-edge region is measured within the first ~6 min) our analyses would have overestimated melt $Fe^{3+}/\Sigma Fe$ by ~0.036. This would correspond to overestimating the fO_2 by 0.5 log units for a basalt at 1150 °C and 400 MPa, according to the model of Kress and Carmichael (1991).

In summary, photo-oxidation during Fe-XANES measurements can cause large systematic biases toward higher calculated $Fe^{3+}/\Sigma Fe$ in beam-sensitive glasses, which can significantly affect geologic interpretations of redox conditions (Cottrell et al., 2018; Moussallam et al., 2019). Taking measures to mitigate beam damage through reduced X-ray flux density (where possible) and/or by applying analysis-specific time-dependent corrections described here is critical for accurate interpretation of Fe-XANES measurements in beam-sensitive glasses, such as hydrous arc basalts. We present a time-dependent correction method and set of analysis conditions that should enable beam damage identification and correction in most natural silicate glasses at even relatively high photon flux densities (10^7–10^8 photons/s/μm^2). However, photo-oxidation during analysis is a function of glass composition (including H_2O content and initial $Fe^{3+}/\Sigma Fe$), photon flux density, and duration of analysis, and therefore depends on the specific sample and beamline properties. Best practices during Fe-XANES analysis of glasses should include explicitly testing (via 2nd pre-edge multiplet dwell tests) whether repeated rapid pre-edge scans sufficiently correct photo-oxidation for the particular beamline conditions and sample compositions being analyzed.

3. Identifying and correcting S-XANES beam damage

S-XANES measurements use lower X-ray energies than Fe-XANES (~2480 eV vs ~7110 eV, respectively) and therefore have smaller absorption lengths than Fe-XANES measurements. At S-XANES energies, 95% of X-ray energy is absorbed within the upper ~15 μm of glass (Wilke et al., 2011) (Fig. 1A). The MI analyzed here are thicker than 15 μm so that doubly intersecting the inclusions was not necessary for S-XANES analyses. Additionally, most host minerals contain negligible sulfur compared to MI (Callegaro et al., 2020) so that beam overlap of the host mineral is less of a concern than for Fe-XANES analyses, where iron signal contribution from the host phase can be significant. Consequently, larger X-ray analysis footprints can generally be used for S-XANES, which reduces X-ray dose and thereby ameliorates some of the beam damage potential. However, when analyzing sulfur-poor MI (<~400 ppm S), even slight contributions from the host phase might be significant relative to the low-sulfur glass signal, and beam overlap of the host phase should be avoided. Additionally, cracks and surface contaminants (e.g., oils) may be present on prepared surfaces, both of which can contain undesired sulfur-bearing material (Brounce et al., 2019). Consequently, smaller beam footprints for S-XANES remain more versatile for analyzing MI (particularly low-sulfur samples) because of the ability to avoid contamination from host minerals or surface aberrations.

Sulfur in silicate melts occurs as S^{2-} (sulfide complexes) or S^{6+} (sulfate complexes; $S^{(VI+)}O_4^{2-}$) but does not naturally occur as S^{4+} (sulfite complexes; $S^{(IV+)}O_3^{2-}$) at the limit of detection by XANES (Backnaes et al., 2008; Wilke et al., 2008, 2011). The main absorption peak of S^{2-} complexes in glasses occurs over a broad energy range centered at ~2476 eV, and the narrower absorption peak of S^{6+} complexes occurs at ~2482 eV (Li et al., 1995; Paris et al., 2001; Bonnin-Mosbah et al., 2002; Wilke et al., 2008; Métrich et al., 2009; Jugo et al.,

2010). In Fe-bearing natural glasses, S-XANES beam damage typically manifests as the photo-reduction of S^{6+} to S^{4+} (Wilke et al., 2008). The absorption peak of sulfite occurs at ~2477.5 eV (note that the rapid oxidation of sulfite at the surface causes a sulfate peak to also be present in the spectra of most sulfite reference materials) (Métrich et al., 2002, 2009; Bonnin-Mosbah et al., 2002; Fleet et al., 2005; Wilke et al., 2008; Jugo et al., 2010). This 2477.5 eV sulfite peak is a unique spectral signal to recognize S^{4+} speciation and thereby can be used to identify measurements that have undergone photo-reduction (Wilke et al., 2008; Métrich et al., 2009; Moussallam et al., 2014). Beam damage is therefore more easily detected in S-XANES than in Fe-XANES, and time-dependent corrections to t = 0 s are not necessary because all observed S^{4+} is generally attributable to beam-induced reduction of sulfur. Photo-reduction of S^{6+} has also been observed during EPMA S-*K*α wavelength scans (Wilke et al., 2008). However, photo-oxidation of S^{2-} to S^{4+} or to S^{6+} has been documented by other EPMA studies (Wallace and Carmichael, 1994; Rowe et al., 2007) and during extremely long duration XANES measurements (20–80 min) of highly alkalic glasses from Mt. Erebus (Antarctica) (Moussallam et al., 2014). The predominance of sulfur photo-reduction during XANES analyses of natural glasses suggests that different mechanisms of sulfur beam damage may occur under electron bombardment compared to X-ray irradiation, and potentially also during X-ray irradiation of certain alkali-rich glasses (Hughes et al., 2020).

The parameters influencing S^{6+} to S^{4+} photo-reduction in silicate glasses during S-XANES irradiation are imprecisely known. In contrast to Fe-XANES beam damage (Cottrell et al., 2018), H_2O content does not appear to be a critical control on S-XANES beam damage (see below), and the compositional dependence of S-XANES beam damage susceptibility has not been thoroughly examined. Consequently, it is difficult to currently predict whether any particular sample will be susceptible to S-XANES beam damage. Therefore, as with Fe-XANES beam damage, it is important to be able to account for S-XANES beam damage in each individual measurement rather than applying generalized corrections to an entire sample suite.

Our approach for managing and correcting S-XANES beam damage is similar to that for reducing Fe-XANES beam damage, namely minimizing pre-analysis X-ray irradiation, decreasing photon dose as much as possible while maintaining sufficient signal, and using repeat rapid scans to observe beam-induced changes in sulfur speciation. Where S-XANES photo-reduction is observed, we correct affected spectra by calculating the peak area of the beam damage-induced S^{4+} signal and restoring this to original S^{6+} intensity via a calibrated conversion factor (details below).

3.1. S-XANES analytical conditions

S-XANES measurements at APS GSECARS beamline 13-ID-E were conducted in fluorescence mode and within a He-environment to minimize atmospheric absorption of the X-ray fluorescent signal. Incident beam flux ranged from ~1–50 × 10^9 photons/s for S-XANES analyses, which was purposely lowered from the maximum possible flux to reduce rates of beam damage. Repeat measurements of sulfate within Scotch® tape during four analytical sessions between 2017 and 2020 indicate a consistent S^{6+} peak position of 2481.8 eV. The sulfate peak position in crystalline hauyne measured by Jugo et al. (2010) at the European Synchrotron Radiation Facility's beamline ID21 is +1 eV relative to sulfate measurements at APS beamline 13-ID-E, due to differences in monochromator calibration (Head et al., 2018). Thus, all the Jugo et al. (2010) values presented in figures and data tables have been shifted by −1 eV for consistency with the APS measurements.

As with our Fe-XANES beam damage correction approach, we conducted repeat rapid scans to identify S-XANES beam damage and, if necessary, applied sample-specific corrections. Sulfur *K*-edge spectra were collected by scanning the incident beam from 2437 to 2467 eV in 2.5 eV steps, from 2467 to 2487 eV in 0.1 eV steps, and from 2487 to 2622 eV in 1.5 eV steps. Short analysis times of either 0.5 or 1.0 s per step bin were used (continuous steps rather than discrete) for rapid scans with total durations of 154 or 308 s, respectively. Three repeat scans were typically conducted for each analysis spot, with cumulative measurement times of ~8–15 min per location. If S^{4+} peak growth was identified during successive scans, only the first scan was used to quantify sulfur speciation, as this scan would have undergone the least S^{6+} to S^{4+} photo-reductive beam damage. If no S^{4+} peak ingrowth was observed, the repeat scans were merged to improve signal quality.

In beam-damaged samples, S^{6+} to S^{4+} photo-reduction can be corrected by restoring the S^{4+} 2477.5 eV peak intensity back to a S^{6+} signal. This correction requires knowing an appropriate scaling factor to restore S^{4+} signal intensity to the original S^{6+} intensity. Konecke et al. (2017) and Nash et al. (2019) apply S-XANES beam damage corrections by assuming a 1:1 intensity scaling between S^{4+} and S^{6+} peaks. However, in the absence of direct evidence, the accuracy of this assumed 1:1 scaling relationship of fluorescent energy outputs is uncertain. To determine how the loss of S^{6+} intensity relates to the growth of S^{4+}, and therefore how to calculate an appropriate signal intensity scaling factor between these peak intensities, we conducted a series of measurements on a hydrous, sulfur-rich experimental basaltic glasses from Chowdhury and Dasgupta (2019) that contain sulfur exclusively as sulfate (Table 1). The large area of this experimental glass allowed a series of measurements with multiple spot sizes (2 × 2, 10 × 10, 20 × 20, and 50 × 50 μm) to observe varying degrees of beam damage under photon densities ranging from 6.9 × 10^6 to 1.1 × 10^{10} photons/s/μm^2. The sulfate-only initial composition of this oxidized glass made the identification of S^{4+} peak ingrowth obvious. With repeat measurements, we are able to track the ingrowth of the S^{4+} 2477.5 eV peak (hereafter the "S^{4+} peak") at the expense of the S^{6+} peak. We can thereby quantify how the S^{4+} peak intensity relates to the loss of S^{6+} intensity, and how consistent the S^{4+} to S^{6+} intensity scaling relationship is with increasing degrees of beam damage.

3.2. Quantifying S-XANES spectra via peak fitting

Determining the relationship between S^{4+} signal growth and S^{6+} signal loss during S-XANES beam damage requires a consistent peak fitting method to quantify the absorption intensities. Peak fitting approaches to S-XANES spectra have been employed by other researchers (Manceau and Nagy, 2012; Konecke et al., 2017; Nash et al., 2019), but have not been described or calibrated in silicate glasses at the level of detail required to be fully reproducible. We therefore establish a new peak fitting calibration based on the dataset used by Jugo et al. (2010) to originally define a calibration relating S-XANES signal intensities to sulfur speciation. S-XANES spectra of silicate glasses are produced by a mixture of X-ray photon absorptions by S^{2-}, S^{4+}, and S^{6+} species, and by S^{1-} and S^{2-} sulfide complexes (Paris et al., 2001; Fleet et al., 2005; Métrich et al., 2009). Jugo et al. (2010) empirically determined a relationship of S^{2-} and S^{6+} X-ray absorption intensities to sulfur speciation using a set of experimental glasses by integrating all signal within energy ranges relating to S^{2-} and S^{6+} peaks (2474.7–2479 eV and 2480.5–2483 eV, respectively; Jugo et al., 2010 ranges have been shifted by −1 eV). However, the S^{4+} absorption peak occurs within the broad S^{2-} energy range. Consequently, the Jugo et al. (2010) approach would inappropriately count photo-reduction-induced S^{4+} signal intensity as S^{2-} intensity. Our peak fitting approach differentiates S^{2-}, S^{4+}, and S^{6+} absorption intensities, enabling us to quantify beam damage by isolating the S^{4+} peak from the S^{2-} peak. We can then restore the S^{4+} photo-reduction signal to the original S^{6+} intensity to calculate the initial sulfur speciation of the glass.

Our S-XANES peak fitting method again uses the spectral fitting program XAS viewer (Newville, 2013) to correct for instrument deadtime and fit the S-XANES data. Measured spectra were first normalized to the Si-*K*α signal intensity, to avoid irregularities in incident beam intensity due to possible contaminants within the beamline optics.

Following the approach of Jugo et al. (2010) and Anzures et al. (2020), we then normalize each spectrum so that the energy range containing pre-edge features begins at zero intensity (~2467 eV) and the post-edge signal intensity is 1 (>2510 eV). This is done by defining a linear relation in the low energy range (~2441–2467 eV), and flattening the high energy range (~2525–2611 eV) to scale the spectra to between 0 and 1 (Ravel and Newville, 2005; Anzures et al., 2020). These energy ranges for normalization are guidelines that should be slightly modified as necessary if anomalous data points are present for particular scans. However, sulfide X-ray absorption begin at energies just above 2467 eV, so the pre-edge normalization range should be kept below this energy. The normalized post-edge spectrum is fit using an error function and a broad Gaussian, which together define the background. The center point of the error function is fixed and the width of the high-energy Gaussian is constrained to maintain a consistent background fitting approach for all spectra (Table 2).

Assessing S-XANES spectra of >100 reduced and oxidized glass analyses across a compositional range from basaltic to rhyolitic (Table 1; Data supplement), we identify the energy ranges of five peaks within the S-*K*α absorption region. We distinguish four absorption peak ranges that have been recognized as corresponding to sulfide complexes, and S^{2-}, S^{4+}, and S^{6+} species (Wilke et al., 2008, 2011; Métrich et al., 2009; Jugo et al., 2010; Head et al., 2018) (Table 2). We additionally identify an absorption peak between 2483.5 and 2486 eV, which is slightly higher energy than the main S^{6+} peak. This 2483.5–2486 eV energy peak was similarly identified by Konecke et al. (2017), who refer to it as the sulfur "ionization peak", a term we adopt here. The sulfur-ionization peak intensity seems partially correlated to S^{6+} intensity, but is also present in S^{2-}-dominated spectra. After normalizing the spectra, we simultaneously fit the background with an error function and Gaussian and fit five separate Gaussian functions for each of the sulfur absorption features (Fig. 7, Fig. A.6). Table 2 provides the energy ranges and peak width tolerances for fitting each spectral feature. These fitting ranges have been established to provide flexibility in fitting slight differences in peak energies occurring across a range of compositions and oxidation states, while maintaining peak positions that accurately correspond to the specific sulfur features (important for overlapping features such as the S^{2-} and S^{4+} peaks, and the S^{6+} and sulfur ionization peaks).

Table 2
Peak definitions and fit parameters used for quantification of normalized S-XANES spectra intensities using the XAS Viewer spectral fitting program (Newville, 2013). See Data supplement for example peak fit models.

S-XANES feature	Function type/name	Peak center bounds (eV)	Peak sigma bounds (width)	Peak amplitude bounds
Overall fit ranges				
Peak fit range	–	2455–2550	–	–
Pre-edge fit range	–	2466–2487	–	–
Background fitting				
Baseline error function	error1	2485 (fixed)	8 (fixed)	0–1.1
Baseline Gaussian	gauss1	2493–2500	0–10	0–15
Sulfur speciation peaks				
Sulfide complexes	gauss2	2465–2470	0–1	0 – ∞
S^{2-} (sulfide in glass)	gauss3	2475.3–2477	2–4	0 – ∞
S^{4+} (sulfite)	gauss4	2476.8–2477.7	0.1–1	0 – ∞
S^{6+} (sulfate)	gauss5	2480–2482.3	0.1–3	0 – ∞
Sulfur ionization peak	gauss6	2483.5–2486	0–4	0 – ∞

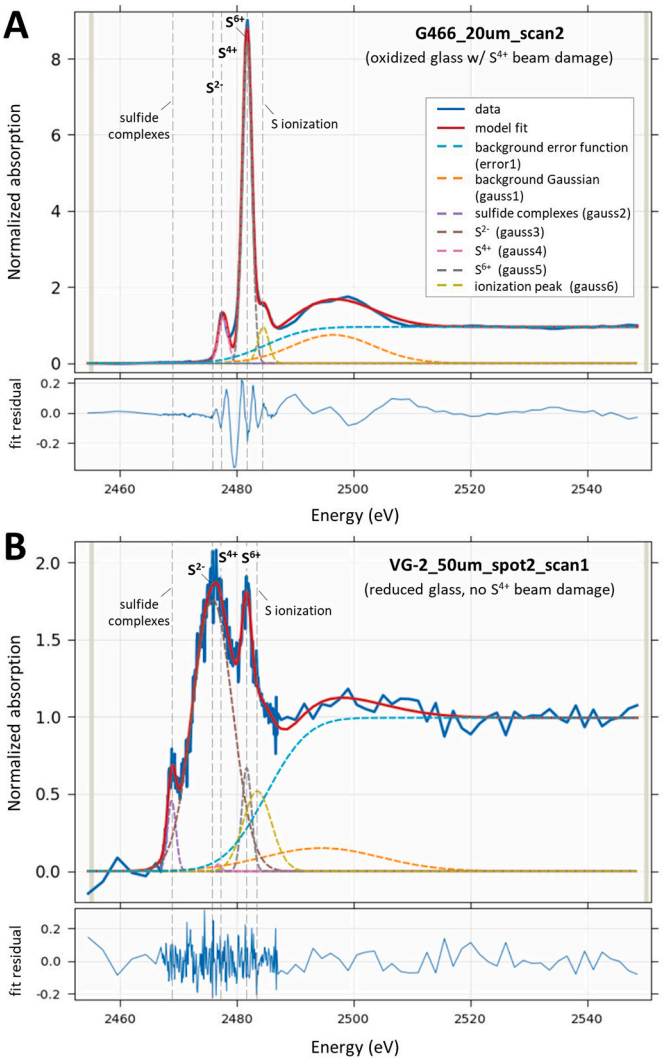

Fig. 7. *(A)* Example S-XANES peak fitting of oxidized experimental glass G466. This spectrum is the 2nd of 3 repeat scans with a 20 × 20 μm beam (photon flux density of 1.1 × 10^8 photons/s/μm^2) and shows a dominant S^{6+} peak (2480–2482.3 eV) and a substantial beam damage-induced S^{4+} peak (2476.8–2477.7 eV). No S^{2-} intensity is observed. The fit residual shows slight remaining unfit structure. *(B)* Example S-XANES peak fitting of reduced VG-2 MORB glass analyzed using a 50 × 50 μm beam (photon flux density of 6.2 × 10^6 photons/s/μm^2). The noisier spectrum is due to lower sulfur content in VG-2 than in G466, as well as a difference in vertical scale. A main glassy S^{2-} peak (2475.3–2477 eV) is present, as well as a lesser S^{6+} peak and a minor sulfide peak (2465–2470 eV). Minimal S^{4+} beam damage ingrowth is observed with this diffuse beam analysis (compare to Fig. 9). A sulfur-ionization peak (2483.5–2486 eV) is present in S-XANES spectra of the both oxidized and reduced glasses. See Table 2 for identification of peaks and fit parameters. Reference peak position lines may vary slightly between samples depending on bond coordination environments.

To relate the fitted peak areas to sulfur speciation, we calibrate our peak fitting method to experimental hydrous basaltic glasses presented in Jugo et al. (2010). Following the same approach as Jugo et al. (2010), we use their completely S^{2-}-bearing and completely S^{6+}-bearing experimental glasses as reduced and oxidized end-members, and apply linear combination fitting of these end-members to produce representative mixed speciation spectra (Fig. A.5). Complete details are provided in the Supplementary information.

Jugo et al. (2010) focus their S-XANES calibration on only S^{2-} and

S^{6+} peak intensities, and do not include signals from lower energy sulfide-complexes or higher energy features beyond the S^{6+} peak. We follow this approach, and although we fit all spectral features in the calibration glasses, we use only the S^{2-} and S^{6+} peak areas to quantify the sulfur speciation in glasses (Fig. 7, Fig. A.6). Jugo et al. (2010) describe an exponential function to relate S^{2-} and S^{6+} peak intensities to sulfur speciation, however we find that the following empirical polynomial relationship is more appropriate for our peak fitting method (Fig. A.7):

$$S^{6+}/\Sigma S = 0.1733*\left(I[S^{6+}]/\Sigma I[S^{T}]\right)^2 + 0.8343*\left(I[S^{6+}]/\Sigma I[S^{T}]\right) \quad (1)$$

where $S^{6+}/\Sigma S$ is the fraction of S^{6+} out of total sulfur in the glass, and $I[S^{6+}]/\Sigma I[S^{T}]$ is the XANES-measured S^{6+} intensity (Gaussian peak area) out of the combined total intensities of the S^{6+} peak and the broad S^{2-} peak ($I[S^{6+}] + I[S^{2-}] = I[S^{T}]$). This peak fitting approach accurately reproduces observations from additional glasses synthesized by Jugo et al. (2010) across a range of fO_2 and sulfur speciation (Fig. A.8). We therefore conclude that our peak fitting approach is similar to the calibration (and this compatible with the thermodynamic relations) originally described by Jugo et al. (2010), while additionally allowing the quantification of a S^{4+} peak. We note that our method is subject to the same limitations as the Jugo et al. (2010) approach, namely, that the linear end-member mixing approach to calibrate mixed sulfur speciation glasses is valid. Additional uncertainty arises from inconsistencies with normalizing S-XANES spectra, which can be challenging in sulfur-poor glasses. Unfortunately, raw S-XANES spectra are seldom published, which precludes assessing consistency in normalization approaches between studies. For reproducibility of spectral processing by future workers, it is important that both the raw and the normalized S-XANES data be made available (see Data supplement) (Rose-Koga et al., 2021).

The average precision of our S-XANES peak fitting method, based on multiple analyses in single MI and within regions of mid-ocean ridge basalt (MORB) glasses, is ±7% relative (2 RSE, 19 analyses in glasses ranging from 0.07 to 0.85 $S^{6+}/\Sigma S$; see Data supplement). When considering further uncertainties in the peak fitting calibration and from the non-uniqueness of spectra normalization (particularly in signal-limited samples), we assume the total accuracy of this method to be better than ±10% relative.

3.3. Correcting S-XANES beam damage

By including the S^{4+} peak in our fitting methodology, we can quantitatively separate the beam damage-induced S^{4+} signal from the overlapping broad S^{2-} peak in S-XANES spectra. This was not possible with the Jugo et al. (2010) method because all signal intensity over this region was considered as S^{2-}, which would lead to spurious results in beam-damaged spectra (Figs. 8, 9). During repeat measurements of hydrous, sulfur-rich, oxidized, anhydrite-saturated experimental basaltic glasses G466 and G479 (50–51 wt% SiO_2, 9000–15,000 ppm S,

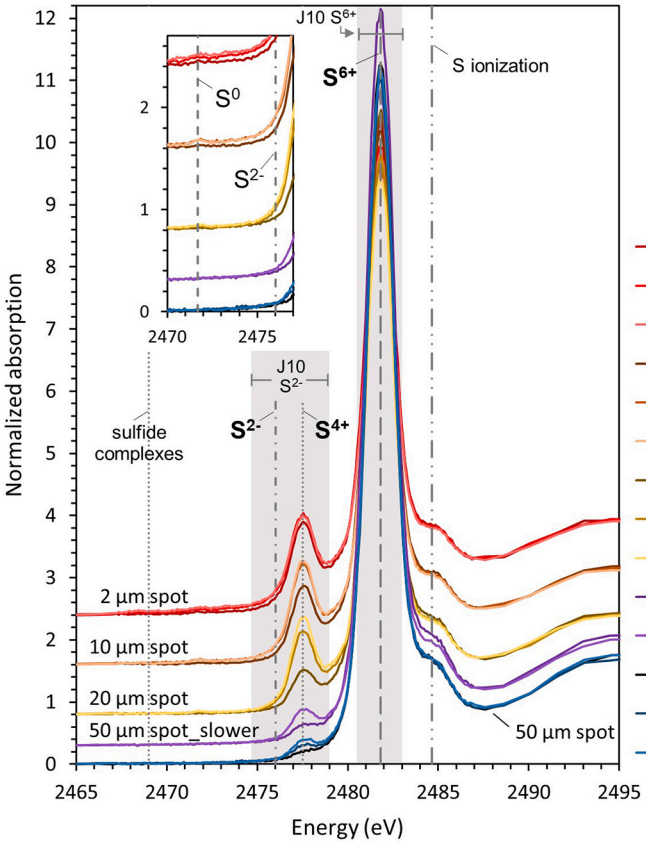

G466 synthetic basalt
(hydrous, oxidized, sulfur-rich)

	$S^{6+}/\Sigma S$ Peak fitting with S^{4+} correction	$S^{6+}/\Sigma S$ Jugo et al. 2010 method
G466_2µm_scan1	1.008	0.663
G466_2µm_scan2	1.008	0.613
G466_2µm_scan3	1.008	0.604
G466_10µm_scan1	1.008	0.738
G466_10µm_scan2	1.008	0.641
G466_10µm_scan3	1.008	0.628
G466_20µm_scan1	1.008	0.872
G466_20µm_scan2	1.008	0.732
G466_20µm_scan3	1.008	0.682
G466_50µm_slower_scan1	1.008	0.975
G466_50µm_slower_scan2	1.008	0.907
G466_50µm_scan1	1.008	1.009
G466_50µm_scan2	1.008	0.980
G466_50µm_scan3	1.008	0.965

Fig. 8. Normalized spectra of oxidized, anhydrite-saturated, experimental glass G466 with repeat measurements in different locations with progressively greater photon flux densities (6.2×10^6, 4.3×10^6, 1.1×10^8, 4.2×10^8, and 1.1×10^{10} photons/s/µm^2 for the 50 µm, 50µm_slower, 20 µm, 10 µm, and 2 µm scans, respectively). Spectra have been vertically shifted for clarity. The ingrowth of S^{4+} (2476.8–2477.7 eV) at the expense of S^{6+} (2480–2482.3 eV) is seen in repeat measurements at all spot sizes, and is increasingly pronounced with more focused beams. S^{4+} ingrowth stops after reaching a maximum intensity during the first focused 2 × 2 µm spot analysis, with no further ingrowth during subsequent analyses. *(inset)* Detailed view of the 2470–2476 eV region showing the ingrowth of a small peak at ~2471.7 eV and a slight absorption increase across 2470–2475 eV in analyses with focused beams. Each individual scan length was 5 min, except for the "G466_50um_slower" scans that were each 10 min. $S^{6+}/\Sigma S$ calculations using the peak fitting approach and correcting for S^{4+} photo-reduction are compared with $S^{6+}/\Sigma S$ calculated using the Jugo et al. (2010) method ("J10" gray S^{2-} and S^{6+} regions [energy shifted as discussed]), where the S^{4+} photo-reduction peak would be counted as part of the S^{2-} signal. Reference peak position lines may vary slightly between samples.

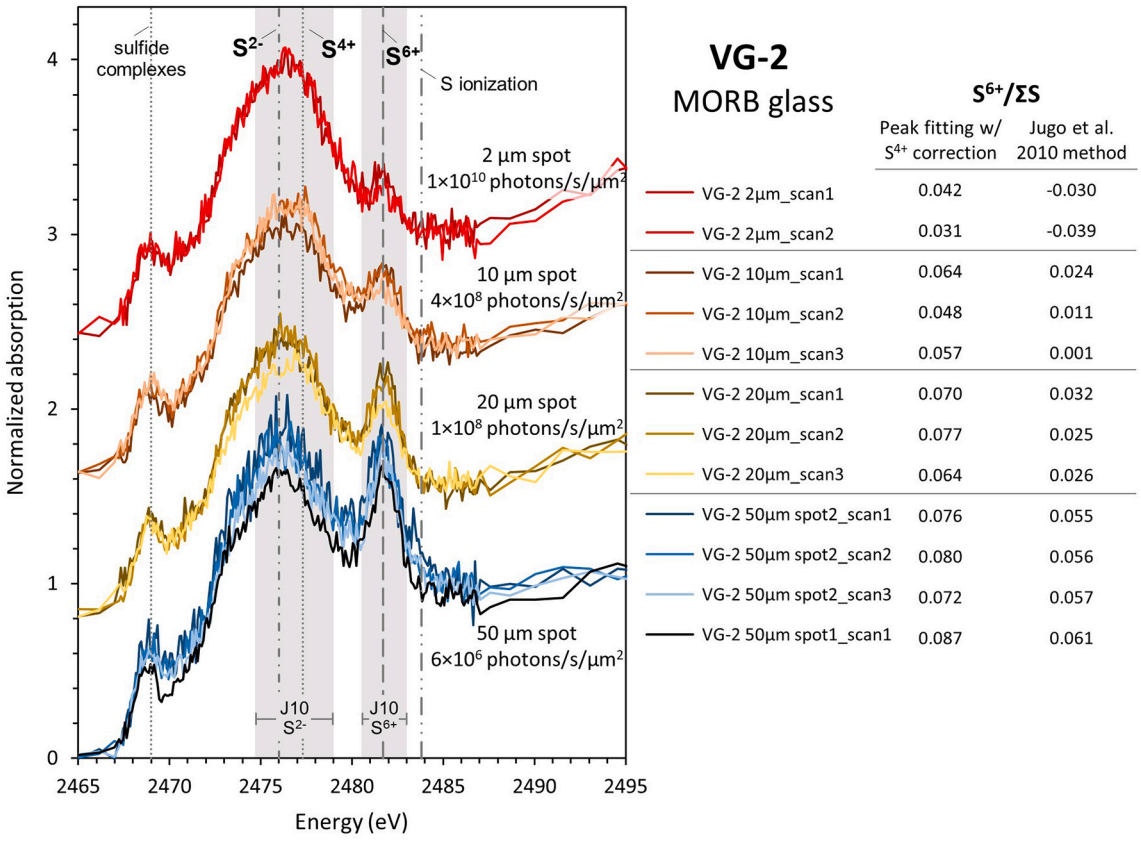

Fig. 9. Normalized S-XANES spectra of MORB glass standard VG-2 with repeat measurements in different locations using progressively greater photon flux densities (6.4×10^6, 1.1×10^8, 4.3×10^8, 1.1×10^{10} photons/s/µm^2 for the 50 µm, 20 µm, 10 µm, and 2 µm scans, respectively). Spectra have been vertically shifted for clarity. The ingrowth of S^{4+} (2476–2477.7 eV) and loss of S^{6+} (2480.5–2483.3 eV) is increasingly apparent during analysis with more focused beams. Measurements with a fully focused 2 × 2 µm beam cause the S^{6+} signal to be almost completely lost. Note the difficulty of recognizing the S^{4+} peak against the dominant S^{2-} broad peak at 2472–2480 eV, giving the illusion of beam damage-free spectra. Each individual scan duration was 5 min. $S^{6+}/\Sigma S$ calculations using the peak fitting approach and correcting for S^{4+} photo-reduction are compared with $S^{6+}/\Sigma S$ calculated using the Jugo et al. (2010) method ("J10" gray S^{2-} and S^{6+} regions [energy shifted as discussed]), where the S^{4+} photo-reduction peak would be counted as part of the S^{2-} signal. Reference peak position lines may vary slightly between samples.

6.5–8.9 wt% H_2O, 1300–1325 °C, 1.5–2.0 GPa; Table 1; Chowdhury and Dasgupta, 2019), we observe that progressive irradiation leads to increasing S^{4+} intensity and concomitant decreasing S^{6+} intensity (Fig. 8) (Wilke et al., 2008; Métrich et al., 2009; Konecke et al., 2017). Because these glasses are highly oxidized, they contain no S^{2-} signal to overlap with the S^{4+} peak, which makes observation of the S^{4+} signal straightforward. As expected, increased photon doses with more focused beams cause more rapid S^{6+} to S^{4+} photo-reduction. Comparing the intensity ratio of S^{4+} peak ingrowth and S^{6+} peak loss during progressive beam damage from repeat measurements with photon flux densities ranging from 10^6 to 10^{10} photons/s/µm^2, we find that S^{4+} peak ingrowth relates to S^{6+} intensity decrease by a factor of 1.2 ± 0.1 (1 SE; $n = 7$) (see Data supplement). We apply this scaling factor to observed S^{4+} peak intensities in beam damaged samples to restore original S^{6+} peak intensities via:

$$\Sigma I[S^{6+}] = (I[S^{4+}] * F_S^{4+/6+}) + I[S^{6+}] \quad (2)$$

where $\Sigma I[S^{6+}]$ is the restored total S^{6+} S-XANES intensity, $I[S^{4+}]$ and $I[S^{6+}]$ are the measured Gaussian peak areas from S-XANES intensities, and $F_S^{4+/6+}$ is the S^{4+} to S^{6+} intensity scaling factor (1.2 ± 0.1; though this may be compositionally dependent, as discussed below). The ratio of S^{6+} signal intensity to total sulfur intensity is then:

$$I[S^{6+}]/\Sigma I[S^T] = \Sigma I[S^{6+}]/(I[S^{2-}] + \Sigma I[S^{6+}]) \quad (3)$$

Inputting this value into our peak fitting calibration based on the Jugo et al. (2010) glass suite (Eq. (1)) calculates the beam damage-restored sulfur speciation.

In addition to the obvious S^{4+} peak growth during beam damage of G466 and G479 glasses, we observe the ingrowth of a very small peak between 2471.6 and 2472.0 eV (Fig. 8 inset), which is in the energy absorption range attributed to S^0 (Fleet et al., 2005; Métrich et al., 2009) or H_2S (Klimm et al., 2012a). This 2471.6–2472.0 eV peak is recognized during successive analyses using 2 × 2, 10 × 10, and 20 × 20 µm spots (10^{10} to 10^8 photons/s/µm^2), but is a negligible feature compared to the S^{4+} and S^{6+} signals. We also observe a slight absorption increase in the broad energy range between 2470 and 2475 eV, which overlaps the S^{2-} glassy absorption range. These subtle features are not included in our beam damage correction approach, as peak-fitting such low-intensity features was inconsistent and sensitive to slight variations in the spectra normalization routine. However, these additional features of S-XANES beam damage invite future investigation.

3.4. Observations of natural glasses and melt inclusions

We observe rapid photo-reduction of S^{6+} to S^{4+} in numerous natural glasses. Hydrous basaltic MI from the southern Cascades (up to 3.7 wt% H_2O) undergo rapid photo-reduction (Muth and Wallace, 2021), which is consistent with hydrous basalts being highly susceptible to speciation changes during X-ray irradiation (Cottrell et al., 2018; Moussallam et al., 2019). However, we also observe rapid photo-reduction during S-XANES analyses of low-H_2O tholeiitic basaltic glasses that have been observed to be very stable during Fe-XANES analyses (Cottrell et al., 2009; Zhang et al., 2018). For example, repeated rapid S-XANES scans of the MORB glass standard VG-2 (NMNH 111240–52; Juan de Fuca ridge)

show a marked decrease in S^{6+} and ingrowth of S^{4+} during successive analyses (Fig. 9). S-XANES measurements of VG-2 have been presented elsewhere (e.g., Head et al., 2018), but have typically been analyzed with a more focused beam and longer measurement times than used here, which we observe to cause a near complete conversion of S^{6+} to S^{4+}. VG-2 glass is relatively reduced (0.15 $Fe^{3+}/\Sigma Fe$, fayalite-magnetite-quartz buffer [FMQ] +0.0; Zhang et al., 2018) so that the original S^{6+} is low and the photo-reduction-produced S^{4+} peak is correspondingly small. The small S^{4+} peak is therefore difficult to discern from the dominant S^{2-} peak, which potentially explains why beam damage in VG-2 glass has not been previously recognized. A North Pacific MORB glass analyzed via S-XANES with a defocused beam by Métrich et al. (2009) also had a recognizable small S^{6+} peak, consistent with our observations of VG-2. Applying our peak fitting and S^{4+} to S^{6+} correction approach to the least beam-damaged VG-2 analyses (50 × 50 μm spot size; 1.1 × 10^7 photons/s/μm^2 flux density), we estimate that VG-2 MORB glass has 0.079 ± 0.007 $S^{6+}/\Sigma S$ (2 SE, n = 4). S-XANES measurements of two additional MORB glasses, JDF-46 N and ALV892–1

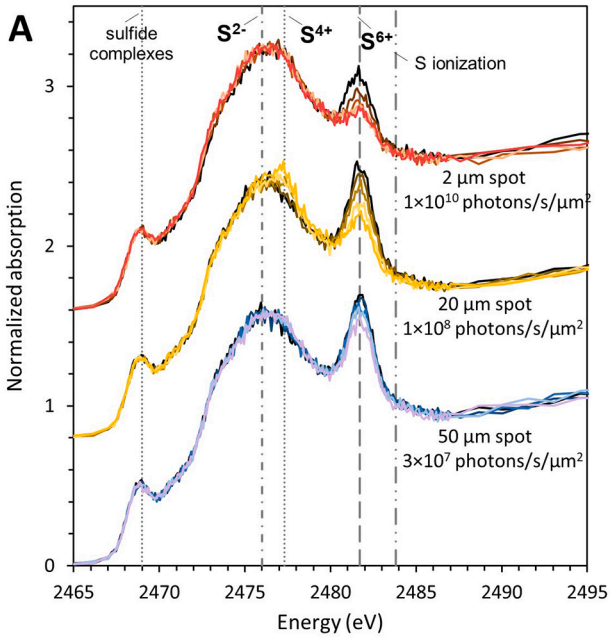

JDF-46N MORB glass	Total analysis time (s)	$S^{6+}/\Sigma S$ Peak fitting with S^{4+} correction	$S^{6+}/\Sigma S$ Peak fitting w/ no S^{4+} correction
JDF-46N 2μm_scan1	304	0.062	0.055
JDF-46N 2μm_scan2	622	0.052	0.043
JDF-46N 2μm_scan5	1575	0.035	0.034
JDF-46N 2μm_scan10	3168	0.037	0.036
JDF-46N 2μm_scan20	6351	0.044	0.041
JDF-46N 20μm_scan1	304	0.082	0.082
JDF-46N 20μm_scan2	622	0.077	0.075
JDF-46N 20μm_scan5	1575	0.069	0.064
JDF-46N 20μm_scan10	3168	0.061	0.051
JDF-46N 20μm_scan20	6351	0.053	0.039
JDF-46N 50μm_scan1	304	0.084	0.084
JDF-46N 50μm_scan2	622	0.077	0.077
JDF-46N 50μm_scan5	1575	0.080	0.078
JDF-46N 50μm_scan10	3168	0.071	0.070
JDF-46N 50μm_scan20	6351	0.072	0.068

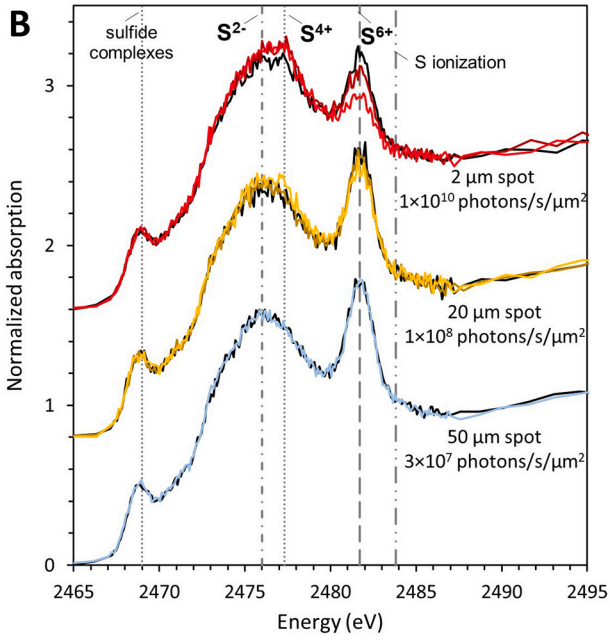

ALV892-1 MORB glass	Total analysis time (s)	$S^{6+}/\Sigma S$ Peak fitting with S^{4+} correction	$S^{6+}/\Sigma S$ Peak fitting w/ no S^{4+} correction
ALV892-1 2μm_scan1	152	0.071	0.068
ALV892-1 2μm_scan2	319	0.062	0.054
ALV892-1 2μm_scan6	986	0.048	0.042
ALV892-1 20μm_scan1	152	0.090	0.089
ALV892-1 20μm_scan2	319	0.088	0.088
ALV892-1 20μm_scan6	986	0.081	0.079
ALV892-1 50μm_scan1	304	0.097	0.097
ALV892-1 50μm_scan2	622	0.092	0.092

Fig. 10. Normalized S-XANES spectra of MORB glasses JDF-46 N and ALV892–1 with repeat measurements in different locations using progressively greater photon flux densities. Spectra have been vertically shifted for clarity. Spectra shown are examples from long sequences of repeated analyses (20 repeated scans for JDF-46 N; 2–6 repeated scans for ALV892–1). Cumulative irradiation durations are listed on the right, and $S^{6+}/\Sigma S$ calculations using the peak fitting approach with and without correcting for S^{4+} photo-reduction are compared. As in Fig. 9, the ingrowth of S^{4+} (2476–2477.7 eV) and loss of S^{6+} (2480.5–2483.3 eV) is increasingly apparent during longer analyses and those with more focused beams. Note that S^{4+} corrections do not reproduce the $S^{6+}/\Sigma S$ observed with low photon density measurements, indicating that challenge of applying beam damage corrections in reduced glasses with overlapping S^{2-} and S^{4+} peak areas. Reference peak position lines may vary slightly between samples.

(Woods Hole Oceanographic Institution, Northeast National Ion Microprobe Facility internal standards), at low photon flux densities (2–3 × 10^7 photons/s/μm^2) give similar $S^{6+}/\Sigma S$ of 0.081 ± 0.002 and 0.093 ± 0.002, respectively (2 SE, n = 4 for each glass). Tests at higher photon flux densities (10^8–10^{10} photons/s/μm^2) or with long analysis durations (>6 min) show that JDF-46 N and ALV892–1 also undergo rapid S^{6+} to S^{4+} photo-reduction (Fig. 10), indicating a common susceptibility for X-ray-induced photo-reduction among low-H_2O MORB samples.

The measured 0.08–0.09 $S^{6+}/\Sigma S$ in these three MORB samples are similar to the upper end of the 0.03–0.07 $S^{6+}/\Sigma S$ range measured in MORB glasses via EPMA S-*K*α wavelength shift (Wallace and Carmichael, 1994) (although the EPMA-measured samples may have suffered from electron beam-induced photo-oxidation [Jugo et al., 2010]). These measurements are all elevated compared to the 0.00–0.02 $S^{6+}/\Sigma S$ measured by S-XANES in four MORB glass samples by Jugo et al. (2010). Based on global MORB average fO_2 estimates of FMQ -0.17 ± 0.15 (0.014 ± 0.01 $Fe^{3+}/\Sigma Fe$) by Cottrell et al. (2020) or FMQ +0.1 by Berry et al. (2018), the Jugo et al. (2010) relationship of S^{6+} to fO_2 predicts that MORB glasses should contain almost exclusively sulfide (≤0.01 $S^{6+}/\Sigma S$). However, our observations indicate that MORB glasses are not universally sulfate-free and, at least in the three localities analyzed here, contain low but resolvable S^{6+} (up to 0.09 $S^{6+}/\Sigma S$).

We also observe S^{6+} to S^{4+} photo-reduction during S-XANES analyses of low-H_2O basaltic MI samples from the 2018 lower East Rift Zone (LERZ) fissure eruption of Kīlauea Volcano, HI (≤0.3 wt% H_2O [Lerner et al., 2021]). Depending on the degree of atmospheric interaction prior

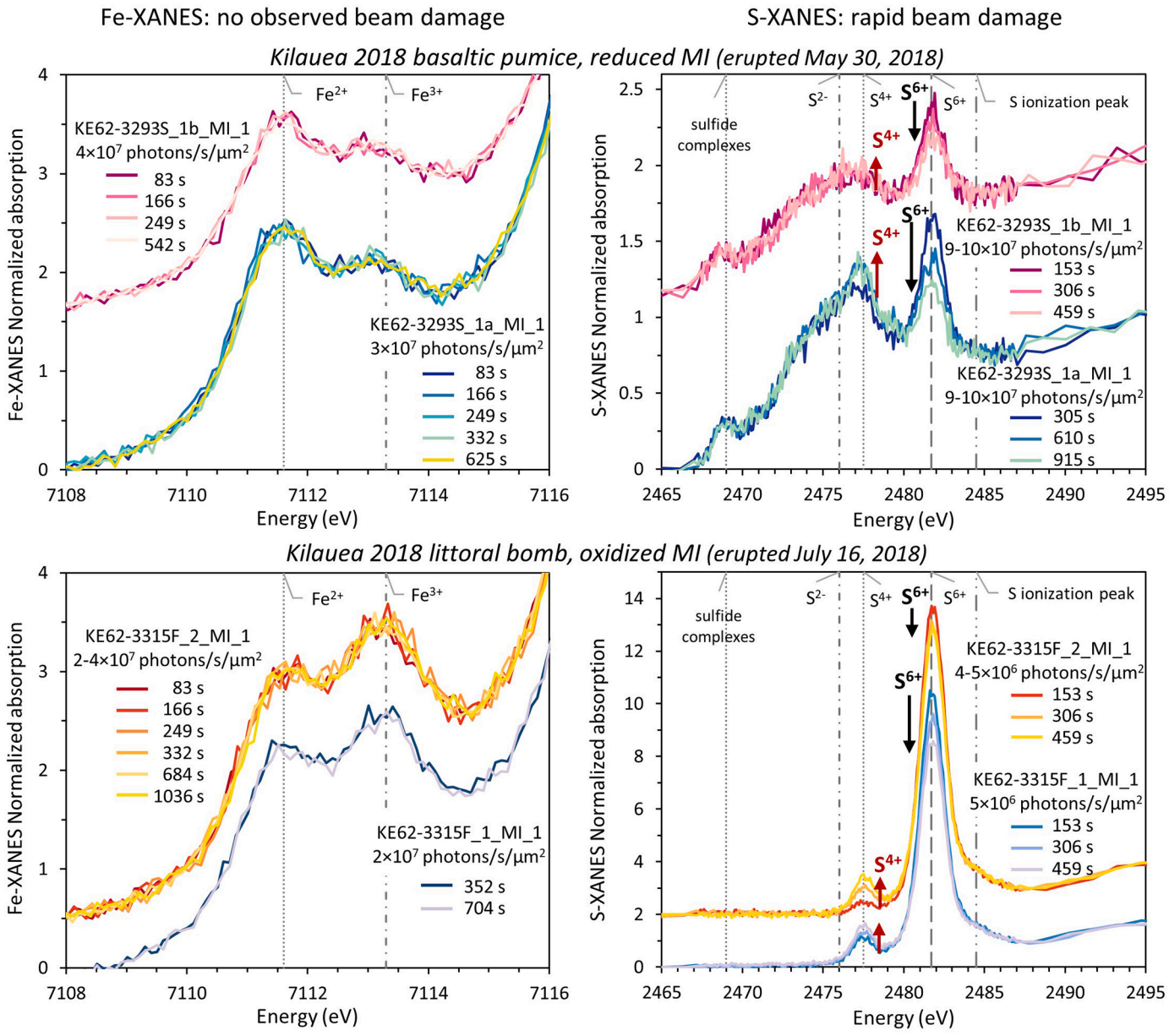

Fig. 11. Four MI from the Kīlauea 2018 LERZ eruption were analyzed by both Fe-XANES *(left)* and S-XANES *(right),* and exhibit differing susceptibilities to Fe- and S-XANES-induced beam damage. Analyses were conducted in different locations within the same MI using repeated rapid analyses for each technique, as described in the text. The cumulative ending time in seconds (s) for successive scans are shown. Melt inclusions in both reduced, rapidly quenched basaltic pumice (KE62-3293S, *top*) and oxidized littoral bomb samples (KE62-3315F, *bottom*) exhibit no Fe^{2+} to Fe^{3+} photo-oxidation during repeat measurements, but the same MI undergo rapid S^{6+} to S^{4+} photo-reduction during S-XANES analyses. All MI contain ≤0.3 wt% H_2O and have Φ <0.1. Spot sizes were 10 × 10 um for Fe-XANES and 10 × 10 or 20 × 20 um for S-XANES resulting in photon flux densities of 2–4 × 10^7 and 4–10 × 10^7 photons/s/μm^2 for Fe- and S-XANES measurements, respectively. Vertical lines are approximate reference peak positions, which may vary slightly between samples.

to quenching, the Kīlauea olivine-hosted MI range from reduced to highly oxidized (FMQ −0.7 to +2.4; Lerner, 2020). S-XANES beam damage occurs in Kīlauea MI throughout this wide range of oxidation states (Fig. 11). The S^{6+} to S^{4+} photo-reduction during X-ray irradiation in Kīlauea MI and in MORB glasses is particularly interesting because these low-H_2O ocean island basalt (OIB) and MORB glasses are stable during Fe-XANES measurements (Fig. 11), having Φ values ≤0.1 (Table 1). These observations highlight that major (e.g., iron) and minor (e.g., sulfur) elements may have different susceptibilities to X-ray-induced beam damage (Gonçalves et al., 2013). Alternatively or additionally, the different responses of iron and sulfur during irradiation may be related to their behavior as non-volatile and volatile elements, or to the ratios of redox couples (e.g., S/Fe concentration ratios) (Hughes et al., 2020).

3.5. Discussion and summary

The S-XANES peak fitting calibration and the determination of the S^{4+} to S^{6+} intensity scaling factor could be improved with calibrations that include different compositions beyond the basalts tested here (experimental glasses of Jugo et al., 2010 and Chowdhury and Dasgupta, 2019). In particular, the concentration of Ca and Fe^{2+} may exert some control on sulfur speciation at given fO_2 conditions and potentially on beam damage susceptibility in glasses (Graz et al., 2007; Klimm et al., 2012a, 2012b). H_2O-content may also play a role in S-XANES beam damage susceptibility (Wilke et al., 2008) as it does in Fe-XANES photo-oxidation (Cottrell et al., 2018). Notably, calculations of sulfur speciation in MORB glasses using the S^{4+} to S^{6+} scaling factor of 1.2 to account for sulfur photo-reduction result in systematically lower $S^{6+}/\Sigma S$ for progressively more beam damaged analyses (from 0.09 to 0.03 $S^{6+}/\Sigma S$) (Figs. 9, 10). This indicates that the S^{4+} to S^{6+} scaling factor is likely larger for H_2O-poor, reduced basalt than what we have determined for hydrous, oxidized basaltic glass. A S^{4+} to S^{6+} scaling factor of >3 is required to equate the $S^{6+}/\Sigma S$ of highly beam damaged MORB analyses with the undamaged measurements made using very low photon flux densities. However, we note that fitting the S^{4+} peak is challenging in more reduced samples due to the overlap of the dominant S^{2-} peak with the relatively minor S^{4+} peak, and we might be under-fitting the S^{4+} peak in the MORB spectra. Additionally, in samples with mixed sulfur speciation, the slight beam damage-induced energy increase in the 2470–2475 eV range (Fig. 8 inset) would be completely masked by, and included within, the broad S^{2-} peak area. Further characterizing the complete range of sulfur complexing and valence changes during beam damage will be important for further improving S-XANES correction methods. The uncertainties in the S^{4+} to S^{6+} intensity corrections underscore that the foremost approach during S-XANES measurements should be to minimize beam damage as much as possible, so that the overall uncertainties stemming from any S^{4+} corrections are small.

In summary, S-XANES beam damage can occur in both hydrous and relatively anhydrous silicate glasses, but can be identified through repeat rapid scans by the presence and growth of a S^{4+} peak. If beam damage is found to occur, we suggest focusing on the least damaged spectra for each measurement, and then applying a S^{4+} to S^{6+} scaling factor to restore S^{4+} signal to the original S^{6+} intensity. In high-sulfur samples, where signal intensity is sufficient even with rapid scans, this is the ideal approach as beam damage is first limited and then restored to a good approximation of original S^{6+} intensity. Low-sulfur samples may require merging multiple rapid scans to obtain quantifiable spectra, despite the longer cumulative analysis time inducing more photo-reduction. In long duration or merged scans, irradiation-induced S^{4+} signal can still be restored to S^{6+} intensity, and although this introduces greater uncertainty (due to imprecisely known S^{4+} to S^{6+} scaling factors), it is still a better approach than not applying any beam damage correction. In highly oxidized samples lacking S^{2-}, accounting for S^{4+} is less important as it can simply be assumed that all sulfur was originally present as S^{6+}. However, in samples with mixed sulfur speciation, separating any S^{4+} photo-reduction signal from the overlapping S^{2-} peak, and restoring the S^{4+} to original S^{6+} is important in accurately determining the initial sulfur speciation of the glass. Best practices may include specifically determining an appropriate S^{4+} to S^{6+} intensity scaling factor for the particular glass compositions being analyzed.

4. Identifying Fe-oxide nanolite crystals in Fe-XANES spectra

In addition to beam damage concerns during XANES analyses of glasses, the possible cryptic occurrence of nanolite crystals in glasses must also be considered to avoid spurious interpretations of XANES spectra. Nanolites are minerals in the sub-micron range that are typically undecipherable with optical microscopes or even with electron microscopes, but can form in MI during quenching under certain conditions. In some settings, dispersed nanolite crystals become large enough to appear as a fine "dust" within MI (Danyushevsky et al., 2002; Wallace et al., 2003). It has been suggested that Fe-oxides and sulfides may form in MI during cooling and/or diffusive H_2O-loss (Danyushevsky et al., 2002; Rowe et al., 2007; Di Genova et al., 2017, 2018, 2020; Head et al., 2018). Di Genova et al. (2017, 2018) observe that Fe-oxide (magnetite) nanolites preferentially occur in H_2O-rich glasses (≥2.5 wt% H_2O) across a range of compositions, suggesting that high H_2O promotes nanolite formation during quenching. This might occur, for example, because increased H_2O lowers the glass transition temperature, resulting in a larger cooling interval in the liquid state for H_2O-rich melts (Deubener et al., 2003). The presence of nanolites complicates XANES, Raman, and EPMA redox measurements in glasses because the bonding coordination in nanolite minerals may lead to different relationships between ion abundances and signal intensities compared to calibrated relationships in glasses.

Fortunately, the short-range ordering of iron and sulfur in mineral phases can be readily detected via XANES and Raman spectral techniques (Wilke et al., 2006; Di Genova et al., 2017, 2018, 2020; Head et al., 2018). Magnetite nanolites have been spectrally identified by Raman measurements in MI from basalts, dacites, and trachytes containing >4.5 wt% FeO^T and ≥ 2.5 wt% H_2O (Di Genova et al., 2017, 2018). Magnetite nanolite abundance correlates with more oxidized (EPMA-calculated) redox states of MI (Hughes et al., 2018), although it is unclear if nanolites actually form in more oxidized MI, or rather that the presence of nanolites affects the redox quantification. Ni-, V-, and S-XANES have been used by Farges et al. (2001) to identify Ni-bearing nanolites in hydrous albitic experimental glasses (≥ 4.5 wt% H_2O) and by Head et al. (2018) to identify V- and S-bearing spinel and sulfide nanolites in natural basaltic MI from Nyamuragira volcano (D.R. Congo). Finally, Fe-XANES has been used by Wilke et al. (2006) to identify the formation of Fe-oxide nanolites during the slow quenching of hydrous haplogranitic experimental glasses (where 0.06–1.5 μm diameter maghemite nanolites were confirmed by TEM).

Here, we build on the observations of Wilke et al. (2006) and show that Fe-XANES measurements can identify the cryptic occurrence of Fe-oxide nanolites in naturally quenched, optically glassy, hydrous MI. We conducted Fe-XANES measurements of doubly-intersected dacitic-rhyolitic MI from the 2006 eruption of Augustine Volcano (AK, USA) that contain 1 - 4 wt% H_2O (Lerner, 2020) and of basaltic MI from Cerro Negro (Nicaragua) that contain 3 - 4 wt% H_2O (Gaetani et al., 2012) (Table 1). A number of these MI contain a sharp absorption peak at ~7129.5 eV that is similar to the absorption edge feature observed in magnetite phenocrysts from both Augustine and oxidized Kīlauea 2018 LERZ samples (Fig. 12). This magnetite-like peak indicates increased crystalline ordering of iron in the glasses due to Fe-oxide nanolites (Wilke et al., 2006). A magnetite-like peak was also observed in Fe-XANES measurements of optically glassy quartz-hosted MI from Central Andean volcanic centers by Grocke et al. (2016), who similarly considered this feature to indicate Fe-oxide nanolite interference.

Melt inclusions in Augustine feldspar and pyroxene grains that contain Fe-oxide (presumably magnetite or maghemite) nanolites are

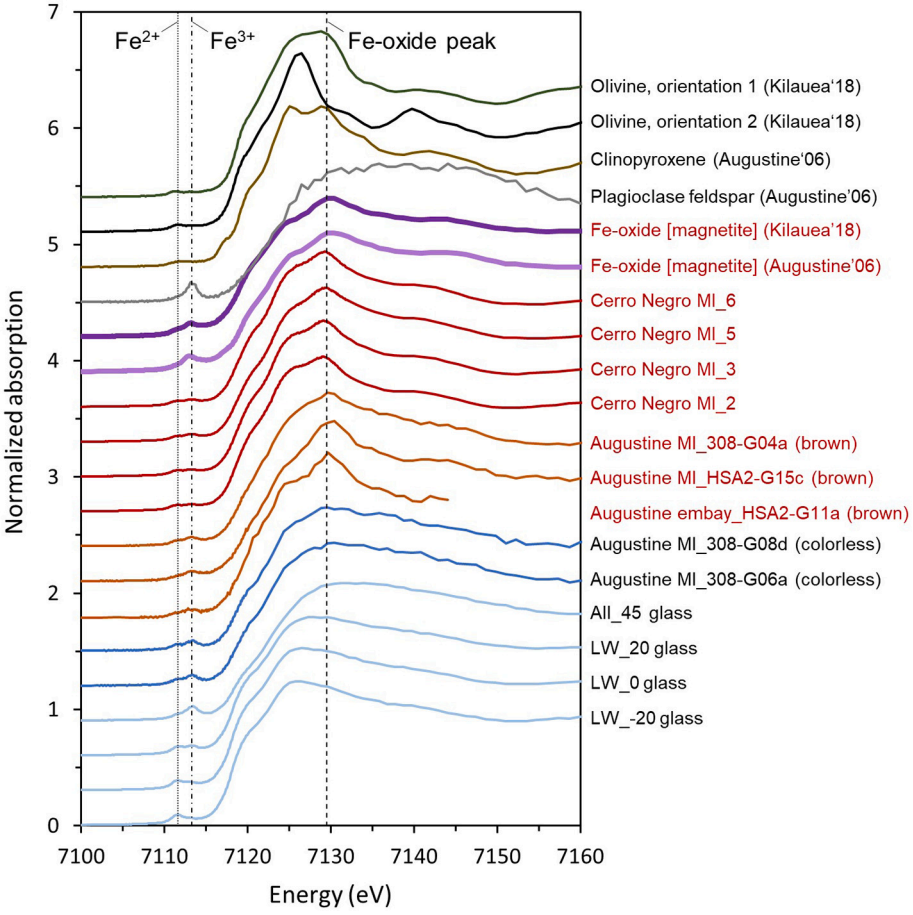

Fig. 12. Normalized Fe-XANES spectra of minerals (olivine, clinopyroxene, feldspar, magnetite), reference glasses (LW series, AII_45; Cottrell et al., 2009), and doubly-intersected MI or melt embayment glasses from Augustine 2006 (samples shown in Fig. 13) and Cerro Negro (see Data supplement). Brown-colored dacitic-rhyolitic glasses from Augustine (orange lines, red labels) have a prominent peak at ~7129.5 eV that closely resemble magnetite spectra (thick purple lines, red labels), indicating the presence of Fe-oxide nanolites. Cerro Negro olivine-hosted basaltic MI (red lines, red labels) also have a 7129.5 eV signature of Fe-oxide nanolites. Colorless MI from Augustine (blue lines) have glassy spectra, similar to oxidized reference glasses LW_20 and AII_45 (FMQ +2 and + 4.5, respectively). Spectra have been vertically shifted for clarity. The lines labeled Fe^{2+} and Fe^{3+} refer to the approximate peak positions of the first and second pre-edge doublet. (For interpretation of the references to color in this figure legend, the reader is referred to the web version of this article.)

consistently a brown color, although no distinct fine-scale crystals are observable with either optical or electron microscopes (Figs. 12, 13). Optically colorless MI are also present in the same samples from Augustine, and these colorless MI have smooth Fe-XANES absorption edge spectra that are indicative of glass with no magnetite-like structure (Figs. 12, 13). The occurrence of colorless and brown MI, even within the same sample, has been long recognized, and the cause and importance of MI glass color has been much debated. Although some studies have found that colorless MI contain lower H_2O and higher CO_2 than co-occurring brown MI, other studies find negligible differences in volatiles or major element compositions between different colored MI (Wallace et al., 1999; Myers et al., 2016; Myers, 2017). However, Fe-XANES analyses show that the color of Augustine MI consistently reflects the presence or absence of magnetite nanolites. These findings are consistent with observations of Fe-oxide (and other crystalline phases) nanolites causing the dark color of natural obsidian and rhyolitic glass (e.g., Sharp et al., 1996; Castro et al., 2005; Ma et al., 2007; Tuffen et al., 2021; Galoisy and Calas, 2021). Iron nanolite-bearing Augustine MI have highly variable calculated $Fe^{3+}/\Sigma Fe$, but in general, these MI are more Fe^{3+}-rich compared to colorless, nanolite-free MI from the same tephra sample (Lerner, 2020). However, it is again unclear whether this observation reflects an increased oxidation state within the nanolite-bearing MI or if it is a consequence of greater Fe^{3+} signal from the crystalline nanolite phases. Importantly, the presence of Fe-oxide nanolites may invalidate the Fe-XANES centroid energy to $Fe^{3+}/\Sigma Fe$ calibrations for glasses. Until further research is undertaken to investigate such effects on XANES calibrations, spectra containing nanolite signatures should be interpreted cautiously. To help focus sample selection and avoid nanolite-induced complications during synchrotron analyses, Raman spectra could be acquired prior to XANES analyses to identify whether nanolites are present in target glasses (Di Genova et al., 2017, 2018).

We note that many brown-colored MI in more basaltic compositions have clean glassy XANES spectra with no evidence of nanolites (e.g., many Kīlauea LERZ and southern Cascades olivine-hosted MI studied here), so MI color alone does not always indicate the presence of Fe-oxide nanolites. Future efforts to characterize compositional, temperature, and H_2O variations between co-occurring brown and colorless MI in the same units will better clarify the processes that govern Fe-oxide nanolite formation and MI glass color.

5. Conclusions and implications

Accurate XANES measurements are essential for inferring magma redox state from iron and sulfur valence states in quenched glasses. Using repeated, rapid Fe- and S-XANES measurements and implementing a new peak-fitting calibration for S-XANES, we have developed time-dependent corrections to identify and correct for beam damage during Fe- and S-XANES analyses of silicate glasses. Beam damage corrections for iron photo-oxidation and sulfur photo-reduction are determined for each individual analysis rather than applying generalized corrections. This allows versatility to account for compositional differences and the effects of variable H_2O concentrations in MI, which can influence beam damage susceptibility. Testing these beam damage correction methods on hydrous experimental basalts, we show that Fe- and S-XANES measurements can be reliably made even on beam-sensitive glasses. Additional studies of the mechanisms and compositional dependence of S-XANES beam damage could further improve the photo-reduction correction method that we have introduced here. Additionally, using Fe-XANES, we demonstrate the occurrence of cryptic Fe-oxide nanolites

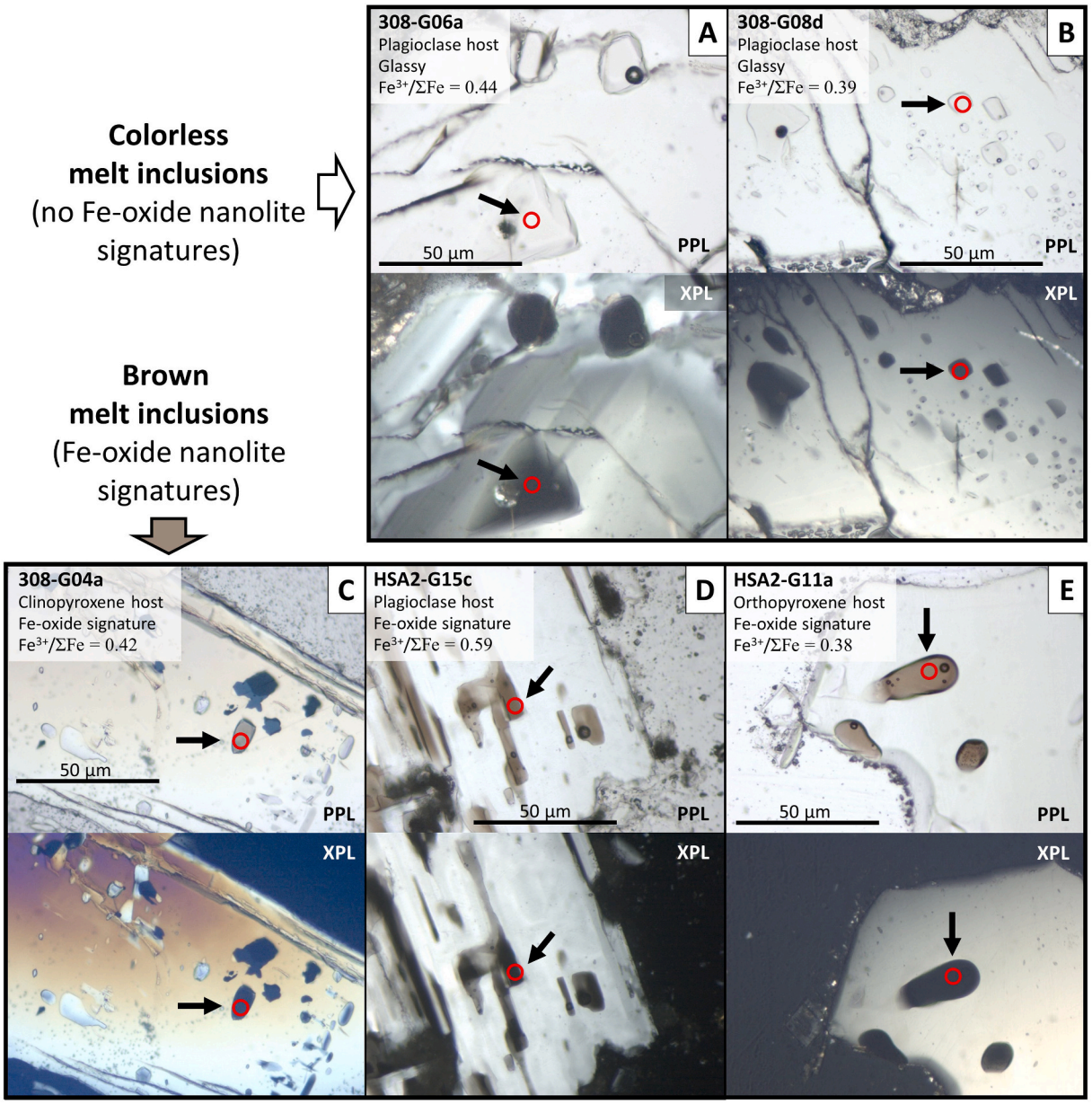

Fig. 13. Doubly-intersected dacitic-rhyolitic MI (A, B, C, D) and melt embayments (E) erupted from Augustine in 2006. *(top)* Colorless glasses (A, B) have completely glassy Fe-XANES spectra whereas *(bottom)* brown glasses have spectral signatures indicating the presence of Fe-oxide nanolites. Each two-pane panel shows images with plane polarized light (PPL) and through crossed polarizers (XPL), with full glass extinction in XPL showing where MI are doubly-intersected for host-free Fe-XANES analysis. All Fe-XANES analyses were conducted with a 5 × 5 µm spot size (~1.4 × 10^8 photons/s/µm^2 flux densities), and spectra are shown in Fig. 12. Photo-oxidation was not observed during repeated analyses in these glasses. $Fe^{3+}/\Sigma Fe$ values were calculated from the felsic glass calibration of Fiege et al. (2017), although we note that the presence of Fe-oxide nanolites in the brown MI may invalidate such $Fe^{3+}/\Sigma Fe$ calculations. (For interpretation of the references to color in this figure legend, the reader is referred to the web version of this article.)

in naturally quenched MI. Melt inclusions containing nanolite phases may invalidate Fe- and S-XANES calibrations for elemental valence and speciation in glasses, and such spectra should be interpreted with caution.

The analytical techniques presented here extend the ability to reliably measure iron valence and sulfur speciation in small and/or hydrous MI, which can undergo substantial beam damage during XANES analyses. These methods will allow further exploration of the redox behavior in hydrous systems, such as magmatic arcs and high-H_2O intraplate volcanic settings. Measurements of redox conditions in magmatic arc glasses are of particular interest in assessing whether subduction inputs oxidize the sub-arc mantle and the relative importance of fO_2 in controlling volcanic degassing and the formation of porphyry copper ore deposits.

We demonstrate that irradiation-induced changes in S-XANES spectra can occur rapidly even in H_2O-poor MORB and OIB glasses that do not experience beam damage during Fe-XANES analysis. This raises the possibility that other multivalent trace element may similarly be subject to beam damage during X-ray analysis, even in relatively anhydrous glasses. The time-dependent analytical techniques presented here can be extended to XANES analyses of other multivalent trace elements, which are being increasingly applied to volcanic glasses (e.g., V-, Cr-, Cu-XANES; Sutton et al., 2020), to assess whether changes in valence or molecular complexing may be occurring during irradiation. Additional research into the mechanisms underlying nanolite formation and irradiation-induced beam damage will continue to improve our

understanding of these phenomena and how they can be better accounted for.

Author contributions

A.H.L. and M.J.M. conceived of the project and led sample preparation, analysis, data synthesis, and authoring. P.J.W., A.L., and M.N. aiding in project design, data interpretation, and manuscript editing. G. A.G., P.C., and R.D. aided in sample preparation and manuscript editing.

Declaration of Competing Interest

The authors declare that they have no known competing financial interests or personal relationships that could have appeared to influence the work reported in this paper.

Acknowledgements

This manuscript was significantly improved thanks to constructive input from M. Wilke and C. Le Losq. We thank D. Dingwell for editorial handling. We thank D. Johnston and J. Watkins (University of Oregon), the U.S. Geological Survey's Hawaiian Volcano Observatory, and the Smithsonian Institution's Department of Mineral Sciences for access to some of the samples analyzed in this study. We also thank J. Donovan and J. Chouinard (University of Oregon) for EPMA assistance. This research used resources of the Advanced Photon Source, a U.S. Department of Energy (DOE) Office of Science User Facility operated for the DOE Office of Science by Argonne National Laboratory under Contract No. DE-AC02-06CH11357. We acknowledge the support of GeoSoilEnviroCARS at the Advanced Photon Source, which is supported by NSF - Earth Sciences (EAR-1128799), and the Department of Energy, Geosciences (DE-FG02-94ER14466). A.H.L and M.J.M. acknowledge support from the National Science Foundation Graduate Research Fellowship Program (NSF-GRFP) under grant 1309047 and internships provided through the Graduate Research Internship Program (GRIP). P. J.W. acknowledges funding support from the National Science Foundation under grant EAR-1834959. Any findings and conclusions or recommendations expressed in this material are those of the authors and do not necessarily reflect the views of the National Science Foundation.

Appendix A. Supplementary data

Supplementary data to this article can be found online at https://doi.org/10.1016/j.chemgeo.2021.120610.

References

Anzures, B.A., Parman, S.W., Milliken, R.E., Lanzirotti, A., Newville, M., 2020. XANES spectroscopy of sulfides stable under reducing conditions. Am. Mineral. 105, 375–381.

Backnaes, L., Stelling, J., Behrens, H., Goettlicher, J., Mangold, S., Verheijen, O., Beerkens, R.G.C., Deubener, J., 2008. Dissolution Mechanisms of Tetravalent Sulphur in Silicate Melts: Evidences from Sulphur K Edge XANES Studies on Glasses. J. Am. Ceram. Soc. 91, 721–727.

Bajt, S., Sutton, S.R., Delaney, J.S., 1994. X-ray microprobe analysis of iron oxidation states in silicates and oxides using X-ray absorption near edge structure (XANES). Geochim. Cosmochim. Acta 58, 5209–5214.

Baker, D.R., Moretti, R., 2011. Modeling the solubility of sulfur in magmas: a 50-year old geochemical challenge. Rev. Mineral. Geochem. 73, 167–213.

Barnes, J.D., Prather, T.J., Cisneros, M., Befus, K., Gardner, J.E., Larson, T.E., 2014. Stable chlorine isotope behavior during volcanic degassing of H_2O and CO_2 at Mono Craters, CA. Bull. Volcanol. 76, 805.

Berry, A.J., O'Neill, H.St.C., Jayasuriya, K.D., Campbell, S.J., Foran, G.J., 2003. XANES calibrations for the oxidation state of iron in a silicate glass. Am. Mineral. 88, 967–977.

Berry, A.J., Danyushevsky, L.V., O'Neill, H.S.C., Newville, M., Sutton, S.R., 2008. Oxidation state of iron in komatiitic melt inclusions indicates hot Archaean mantle. Nature 455, 960.

Berry, A.J., Stewart, G.A., O'Neill, H.S.C., Mallmann, G., Mosselmans, J.F.W., 2018. A re-assessment of the oxidation state of iron in MORB glasses. Earth Planet. Sci. Lett. 483, 114–123.

Bonnin-Mosbah, M., Simionovici, A.S., Métrich, N., Duraud, J.-P., Massare, D., Dillmann, P., 2001. Iron oxidation states in silicate glass fragments and glass inclusions with a XANES micro-probe. J. Non-Cryst. Solids 288, 103–113.

Blundy, J., Melekhova, E., Ziberna, L., Humphreys, M.C.S., Cerantola, V., Brooker, R.A., McCammon, C.A., Pichavant, M., Ulmer, P., 2020. Effect of redox on Fe–Mg–Mn exchange between olivine and melt and an oxybarometer for basalts. Contrib. to Mineral. Petrol. 175 (11) https://doi.org/10.1007/s00410-020-01736-7.

Bonnin-Mosbah, M., Métrich, N., Susini, J., Salomé, M., Massare, D., Menez, B., 2002. Micro X-ray absorption near edge structure at the sulfur and iron K-edges in natural silicate glasses. Spectrochim. Acta B At. Spectrosc. 57, 711–725.

Borisov, A., Behrens, H., Holtz, F., 2018. Ferric/ferrous ratio in silicate melts: a new model for 1 atm data with special emphasis on the effects of melt composition. Contrib. Mineral. Petrol. 173, 98.

Botcharnikov, R.E., Linnen, R.L., Wilke, M., Holtz, F., Jugo, P.J., Berndt, J., 2011. High gold concentrations in sulphide-bearing magma under oxidizing conditions. Nat. Geosci. 4, 112–115.

Brounce, M.N., Kelley, K.A., Cottrell, E., 2014. Variations in $Fe^{3+}/\Sigma Fe$ of Mariana Arc basalts and mantle wedge fO_2. J. Petrol. 55, 2513–2536.

Brounce, M.N., Stolper, E., Eiler, J., 2017. Redox variations in Mauna Kea lavas, the oxygen fugacity of the Hawaiian plume, and the role of volcanic gases in Earth's oxygenation. Proc. Natl. Acad. Sci. 114, 8997–9002.

Brounce, M.N., Boyce, J., McCubbin, F.M., Humphreys, J., Reppart, J., Stolper, E., Eiler, J., 2019. The oxidation state of sulfur in lunar apatite. Am. Mineral. 104, 307–312.

Browaeys, J., 2021. Linear fit with both uncertainties in x and in y. In: MATLAB Central File Exchange.

Callegaro, S., Geraki, K., Marzoli, A., Min, A.D., Maneta, V., Baker, D.R., 2020. The quintet completed: the partitioning of sulfur between nominally volatile-free minerals and silicate melts. Am. Mineral. 105, 697–707.

Carroll, M., Rutherford, M.J., 1988. Sulfur speciation in hydrous experimental glasses of varying oxidation state–results from measured wavelength shifts of sulfur X-rays. Am. Mineral. 73, 845–849.

Castro, J.M., Dingwell, D.B., Nichols, A.R., Gardner, J.E., 2005. New insights on the origin of flow bands in obsidian. In: Manga, M., Ventura, G. (Eds.), Kinematics and Dynamics of Lava Flows, Special Papers-Geological Society of America, 1999. Geological Society of America, Boulder, Colo, pp. 55–65.

Chowdhury, P., Dasgupta, R., 2019. Effect of sulfate on the basaltic liquidus and Sulfur Concentration at Anhydrite Saturation (SCAS) of hydrous basalts–Implications for sulfur cycle in subduction zones. Chem. Geol. 522, 162–174.

Cottrell, E., Kelley, K.A., 2011. The oxidation state of Fe in MORB glasses and the oxygen fugacity of the upper mantle. Earth Planet. Sci. Lett. 305, 270–282.

Cottrell, E., Kelley, K.A., Lanzirotti, A., Fischer, R.A., 2009. High-precision determination of iron oxidation state in silicate glasses using XANES. Chem. Geol. 268, 167–179.

Cottrell, E., Lanzirotti, A., Mysen, B., Birner, S., Kelley, K.A., Botcharnikov, R., Davis, F. A., Newville, M., 2018. A Mössbauer-based XANES calibration for hydrous basalt glasses reveals radiation-induced oxidation of Fe. Am. Mineral. 103, 489–501.

Cottrell, E., Birner, S., Brounce, M.N., Davis, F.A., Waters, L.E., Kelley, K.A., 2020. Oxygen Fugacity across Tectonic Settings. In: Neuville, D.R., Moretti, R. (Eds.), Redox Variables and Mechanisms in Magmatism and Volcanism, AGU Geophysical Monograph. Wiley.

Danyushevsky, L.V., McNeill, A.W., Sobolev, A.V., 2002. Experimental and petrological studies of melt inclusions in phenocrysts from mantle-derived magmas: an overview of techniques, advantages and complications. Chem. Geol. 183, 5–24.

Dauphas, N., Roskosz, M., Alp, E.E., Neuville, D.R., Hu, M.Y., Sio, C.K., Tissot, F.L.H., Zhao, J., Tissandier, L., Médard, E., 2014. Magma redox and structural controls on iron isotope variations in Earth's mantle and crust. Earth Planet. Sci. Lett. 398, 127–140.

de Moor, J.M., Fischer, T.P., Sharp, Z.D., King, P.L., Wilke, M., Botcharnikov, R.E., Cottrell, E., Zelenski, M., Marty, B., Klimm, K., Rivard, C., Ayalew, D., 2013. Sulfur degassing at Erta Ale (Ethiopia) and Masaya (Nicaragua) volcanoes: Implications for degassing processes and oxygen fugacities of basaltic systems. Geochem. Geophys. Geosyst. 14, 4076–4108.

Deubener, J., Müller, R., Behrens, H., Heide, G., 2003. Water and the glass transition temperature of silicate melts. J. Non-Cryst. Solids 330, 268–273.

Di Genova, D., Sicola, S., Romano, C., Vona, A., Fanara, S., Spina, L., 2017. Effect of iron and nanolites on Raman spectra of volcanic glasses: a reassessment of existing strategies to estimate the water content. Chem. Geol. 475, 76–86.

Di Genova, D., Brooker, R.A., Mader, H.M., Drewitt, J.W.E., Longo, A., Deubener, J., Neuville, D.R., Fanara, S., Shebanova, O., Anzellini, S., Arzilli, F., Bamber, E.C., Hennet, L., La Spina, G., Miyajima, N., 2020. In situ observation of nanolite growth in volcanic melt: a driving force for explosive eruptions. Sci. Adv. 6 (39), eabb0413 https://doi.org/10.1126/sciadv.abb0413.

Di Genova, D., Caracciolo, A., Kolzenburg, S., 2018. Measuring the degree of "nanotilization" of volcanic glasses: Understanding syn-eruptive processes recorded in melt inclusions. Lithos 318, 209–218.

Dyar, M.D., McCanta, M., Breves, E., Carey, C.J., Lanzirotti, A., 2016. Accurate predictions of iron redox state in silicate glasses: a multivariate approach using X-ray absorption spectroscopy. Am. Mineral. 101, 744–747.

Elam, W.T., Ravel, B.D., Sieber, J.R., 2002. A new atomic database for X-ray spectroscopic calculations. Radiat. Phys. Chem. 63, 121–128.

Farges, F., Munoz, M., Siewert, R., Malavergne, V., Brown, G.E., Behrens, H., Nowak, M., Petit, P.-E., 2001. Transition elements in water-bearing silicate glasses/melts. Part II. Ni in water-bearing glasses. Geochim. Cosmochim. Acta 65, 1679–1693.

Farges, F., Lefrère, Y., Rossano, S., Berthereau, A., Calas, G., Brown, G.E., 2004. The effect of redox state on the local structural environment of iron in silicate glasses: a

combined XAFS spectroscopy, molecular dynamics, and bond valence study. J. Non-Cryst. Solids 344, 176–188.
Fiege, A., Holtz, F., Shimizu, N., Mandeville, C.W., Behrens, H., Knipping, J.L., 2014. Sulfur isotope fractionation between fluid and andesitic melt: an experimental study. Geochim. Cosmochim. Acta 142, 501–521.
Fiege, A., Ruprecht, P., Simon, A.C., Bell, A.S., Göttlicher, J., Newville, M., Lanzirotti, T., Moore, G., 2017. Calibration of Fe XANES for high-precision determination of Fe oxidation state in glasses: Comparison of new and existing results obtained at different synchrotron radiation sources. Am. Mineral. 102, 369–380.
Fleet, M.E., Liu, X., Harmer, S.L., King, P.L., 2005. Sulfur K-edge XANES spectroscopy: Chemical state and content of sulfur in silicate glasses. Can. Mineral. 43, 1605–1618.
Gaborieau, M., Laubier, M., Bolfan-Casanova, N., McCammon, C.A., Vantelon, D., Chumakov, A.I., Schiavi, F., Neuville, D.R., Venugopal, S., 2020. Determination of $Fe^{3+}/\Sigma Fe$ of olivine-hosted melt inclusions using Mössbauer and XANES spectroscopy. Chem. Geol. 547, 119646.
Gaetani, G.A., O'Leary, J.A., Shimizu, N., Bucholz, C.E., Newville, M., 2012. Rapid reequilibration of H_2O and oxygen fugacity in olivine-hosted melt inclusions. Geology 40, 915–918.
Galoisy, L., Calas, G., 2021. The unique speciation of iron in calc-alkaline obsidians. Chem. Geol. 559, 119925.
Galoisy, L., Calas, G., Arrio, M.A., 2001. High-resolution XANES spectra of iron in minerals and glasses: structural information from the pre-edge region. Chem. Geol. 174, 307–319.
Gonçalves, Ferreira P., de Ligny, D., Lazzari, O., Jean, A., Gonzalez, O.C., Neuville, D.R., 2013. Photoreduction of iron by a synchrotron X-ray beam in low iron content soda-lime silicate glasses. Chem. Geol. 346, 106–112.
Graz, Y., Scaillet, B., Pichavant, M., Gaillard, F., 2007. The effect of sulfur on the Fe^{2+}/Fe^{3+} ratio of MORB and its implications for the redox state of the mantle.
Grocke, S.B., Cottrell, E., de Silva, S., Kelley, K.A., 2016. The role of crustal and eruptive processes versus source variations in controlling the oxidation state of iron in Central Andean magmas. Earth Planet. Sci. Lett. 440, 92–104.
Head, E., Lanzirotti, A., Newville, M., Sutton, S., 2018. Vanadium, sulfur, and iron valences in melt inclusions as a window into magmatic processes: a case study at Nyamuragira volcano, Africa. Geochim. Cosmochim. Acta 226, 149–173.
Helz, R.T., Cottrell, E., Brounce, M.N., Kelley, K.A., 2017. Olivine-melt relationships and syneruptive redox variations in the 1959 eruption of Kīlauea Volcano as revealed by XANES. J. Volcanol. Geotherm. Res. 333, 1–14.
Hughes, E.C., Buse, B., Kearns, S.L., Blundy, J.D., Kilgour, G., Mader, H.M., Brooker, R. A., Balzer, R., Botcharnikov, R.E., Di Genova, D., 2018. High spatial resolution analysis of the iron oxidation state in silicate glasses using the electron probe. American Mineralogist: Journal of Earth and Planetary Materials 103, 1473–1486.
Hughes, E.C., Buse, B., Kearns, S.L., Brooker, R.A., Di Genova, D., Kilgour, G., Mader, H. M., Blundy, J.D., 2020. The microanalysis of iron and sulphur oxidation states in silicate glass-Understanding the effects of beam damage. In: IOP Conference Series: Materials Science and Engineering. IOP Publishing, p. 012014.
Jarosewich, E., Nelen, J.A., Norberg, J.A., 1980. Reference samples for electron microprobe analysis. Geostand. Newslett. 4, 43–47.
Jégo, S., Dasgupta, R., 2014. The fate of sulfur during fluid-present melting of subducting basaltic crust at variable oxygen fugacity. J. Petrol. 55, 1019–1050.
Jugo, P.J., 2009. Sulfur content at sulfide saturation in oxidized magmas. Geology 37, 415–418.
Jugo, P.J., Wilke, M., Botcharnikov, R.E., 2010. Sulfur K-edge XANES analysis of natural and synthetic basaltic glasses: Implications for S speciation and S content as function of oxygen fugacity. Geochim. Cosmochim. Acta 74, 5926–5938.
Kelley, K.A., Cottrell, E., 2009. Water and the oxidation state of subduction zone magmas. Science 325, 605–607.
Kelley, K.A., Cottrell, E., 2012. The influence of magmatic differentiation on the oxidation state of Fe in a basaltic arc magma. Earth Planet. Sci. Lett. 329–330, 109–121.
Kent, A.J., 2008. Melt inclusions in basaltic and related volcanic rocks. Rev. Mineral. Geochem. 69, 273–331.
Klimm, K., Kohn, S.C., Botcharnikov, R.E., 2012a. The dissolution mechanism of sulphur in hydrous silicate melts. II: solubility and speciation of sulphur in hydrous silicate melts as a function of fO_2. Chem. Geol. 322, 250–267.
Klimm, K., Kohn, S.C., O'Dell, L.A., Botcharnikov, R.E., Smith, M.E., 2012b. The dissolution mechanism of sulphur in hydrous silicate melts. I: Assessment of analytical techniques in determining the sulphur speciation in iron-free to iron-poor glasses. Chemical Geology 322, 237–249.
Konecke, B.A., Fiege, A., Simon, A.C., Parat, F., Stechern, A., 2017. Co-variability of S^{6+}, S^{4+}, and S^{2-} in apatite as a function of oxidation state: Implications for a new oxybarometer. Am. Mineral. 102, 548–557.
Kraft, S., Stümpel, J., Becker, P., Kuetgens, U., 1996. High resolution x-ray absorption spectroscopy with absolute energy calibration for the determination of absorption edge energies. Rev. Sci. Instrum. 67, 681–687.
Kress, V.C., Carmichael, I.S., 1991. The compressibility of silicate liquids containing Fe_2O_3 and the effect of composition, temperature, oxygen fugacity and pressure on their redox states. Contrib. Mineral. Petrol. 108, 82–92.
Kuehn, S.C., Froese, D.G., Shane, P.A.R., INTAV Intercomparison Participants, 2011. The INTAV intercomparison of electron-beam microanalysis of glass by tephrochronology laboratories: results and recommendations. Quat. Int. 246, 19–47.
Lanzirotti, A., Lee, L., Head, E., Sutton, S.R., Newville, M., McCanta, M., Lerner, A.H., Wallace, P.J., 2019. Direct measurements of copper speciation in basaltic glasses: understanding the relative roles of sulfur and oxygen in copper complexation in melts. Geochim. Cosmochim. Acta 267, 164–178.
Lerner, A.H., 2020. The depths and locations of magma reservoirs and their consequences for the behavior of sulfur and volcanic degassing. Ph.D. Thesis. University of Oregon.
Lerner, A.H., Wallace, P.J., Shea, T., Mourey, A.J., Kelly, P.J., Nadeau, P.A., Elias, T., Kern, C., Clor, L.E., Gansecki, C., Lee, R.L., Moore, L.R., Werner, C.A., 2021. The petrologic and degassing behavior of sulfur and other magmatic volatiles from the 2018 eruption of Kīlauea, Hawai'i: melt concentrations, magma storage depths, and magma recycling. Bull. Volcanol. 83, 43.
Li, D., Bancroft, G.M., Kasrai, M., Fleet, M.E., Feng, X., Tan, K., 1995. S K- and L-edge X-ray absorption spectroscopy of metal sulfides and sulfates; applications in mineralogy and geochemistry. Can. Mineral. 33, 949–960.
Ma, C., Rossman, G.R., Miller, J.A., 2007. The Origin of Color in "Fire" Obsidian. Can. Mineral. 45, 551–557.
Manceau, A., Nagy, K.L., 2012. Quantitative analysis of sulfur functional groups in natural organic matter by XANES spectroscopy. Geochim. Cosmochim. Acta 99, 206–223.
Masotta, M., Keppler, H., 2015. Anhydrite solubility in differentiated arc magmas. Geochim. Cosmochim. Acta 158, 79–102.
Matjuschkin, V., Blundy, J.D., Brooker, R.A., 2016. The effect of pressure on sulphur speciation in mid-to deep-crustal arc magmas and implications for the formation of porphyry copper deposits. Contrib. Mineral. Petrol. 171, 66.
McCanta, M.C., Dyar, M.D., Rutherford, M.J., Lanzirotti, A., Sutton, S.R., Thomson, B.J., 2017. In situ measurement of ferric iron in lunar glass beads using Fe-XAS. Icarus 285, 95–102.
McCanta, M.C., Dyar, M.D., Lanzirotti, A., Newville, M., Breitenfeld, L.B., 2019. In-situ mapping of ferric iron variations in lunar glasses using X-ray absorption spectroscopy. Am. Mineral. 104, 453–458.
Métrich, N., Wallace, P.J., 2008. Volatile abundances in basaltic magmas and their degassing paths tracked by melt inclusions. Rev. Mineral. Geochem. 69, 363–402.
Métrich, N., Bonnin-Mosbah, M., Susini, J., Menez, B., Galoisy, L., 2002. Presence of sulfite (SIV) in arc magmas: Implications for volcanic sulfur emissions. Geophysical Research Letters 29 (33–1–33–4).
Métrich, N., Berry, A.J., O'Neill, H.S.C., Susini, J., 2009. The oxidation state of sulfur in synthetic and natural glasses determined by X-ray absorption spectroscopy. Geochim. Cosmochim. Acta 73, 2382–2399.
Moussallam, Y., Oppenheimer, C., Scaillet, B., Gaillard, F., Kyle, P., Peters, N., Hartley, M., Berlo, K., Donovan, A., 2014. Tracking the changing oxidation state of Erebus magmas, from mantle to surface, driven by magma ascent and degassing. Earth Planet. Sci. Lett. 393, 200–209.
Moussallam, Y., Edmonds, M., Scaillet, B., Peters, N., Gennaro, E., Sides, I., Oppenheimer, C., 2016. The impact of degassing on the oxidation state of basaltic magmas: a case study of Kīlauea volcano. Earth Planet. Sci. Lett. 450, 317–325.
Moussallam, Y., Longpré, M.-A., McCammon, C., Gomez-Ulla, A., Rose-Koga, E.F., Scaillet, B., Peters, N., Gennaro, E., Paris, R., Oppenheimer, C., 2019. Mantle plumes are oxidised. Earth Planet. Sci. Lett. 527, 115798.
Muth, M.J., Wallace, P.J., 2021. Slab-derived sulfate generates oxidized basaltic magmas in the southern Cascade arc (California, USA). Geology 49 (10), 1177–1181. https://doi.org/10.1130/G48759.1.
Myers, M.L., 2017. Storage, ascent, and release of silicic magma in caldera-forming eruptions. PhD Thesis. University of Oregon.
Myers, M.L., Wallace, P.J., Wilson, C.J., Morter, B.K., Swallow, E.J., 2016. Prolonged ascent and episodic venting of discrete magma batches at the onset of the Huckleberry Ridge supereruption, Yellowstone. Earth Planet. Sci. Lett. 451, 285–297.
Nash, W.M., Smythe, D.J., Wood, B.J., 2019. Compositional and temperature effects on sulfur speciation and solubility in silicate melts. Earth Planet. Sci. Lett. 507, 187–198.
Newville, M., 2013. Larch: An analysis package for XAFS and related spectroscopies. In: Journal of Physics: Conference Series. IOP Publishing, p. 012007.
O'Neill, H.S.C., Berry, A.J., Mallmann, G., 2018. The oxidation state of iron in Mid-Ocean Ridge Basaltic (MORB) glasses: Implications for their petrogenesis and oxygen fugacities. Earth Planet. Sci. Lett. 504, 152–162.
Osborn, E.F., 1959. Role of oxygen pressure in the crystallization and differentiation of basaltic magma. Am. J. Sci. 257, 609–647.
Papike, J.J., Simon, S.B., Burger, P.V., Bell, A.S., Shearer, C.K., Karner, J.M., 2016. Chromium, vanadium, and titanium valence systematics in Solar System pyroxene as a recorder of oxygen fugacity, planetary provenance, and processes. Am. Mineral. 101, 907–918.
Paris, E., Giuli, G., Carroll, M.R., Davoli, I., 2001. The valence and speciation of sulfur in glasses by X-ray absorption spectroscopy. Can. Mineral. 39, 331–339.
Ravel, B., Newville, M., 2005. ATHENA, ARTEMIS, HEPHAESTUS: data analysis for X-ray absorption spectroscopy using IFEFFIT. J. Synchrotron Radiat. 12, 537–541.
Righter, K., Danielson, L.R., Pando, K., Morris, R.V., Graff, T.G., Agresti, D.G., Martin, A. M., Sutton, S.R., Newville, M., Lanzirotti, A., 2013. Redox systematics of martian magmas with implications for magnetite stability. Am. Mineral. 98, 616–628.
Rose, T., Brown, C., 2017. Status of the Smithsonian Microbeam Standards 2017 with a discussion of the venerable VG-2 basalt glass. Microsc. Microanal. 23, 498–499.
Rose-Koga, E.F., Bouvier, A.-S., Gaetani, G.A., Wallace, P.J., Allison, C.M., Andrys, J.A., de la Torre, C.A.A., Barth, A., Bodnar, R.J., Ajj, B.G., Butters, Castillejo A., Chilson-Parks, B., Choudhary, B.R., Cluzel, N., Cole, M., Cottrell, E., Daly, A., Danyushevsky, L.V., Cl, D., Drignon, M.J., France, L., Gaborieau, M., Garcia, M.O., Gatti, E., Genske, F.S., Hartley, Hughes E.C., Iveson, A.A., Johnson, E.R., Jones, M., Kagoshima, T., Katzir, Y., Kawaguchi, M., Kawamoto, T., Kelley, K.A., Koornneef, J. M., Kurz, Laubier M., Layne, G.D., Lerner, A., Lin, K.-Y., Liu, P.-P., Lorenzo-Merino, A., Luciani, N., Magalhães, N., Marschall, H.R., Michael, P.J., Monteleone, B.D., Moore, L.R., Moussallam, Y., Muth, M., Myers, M.L., Narváez, D.

F., Navon, O., Newcombe, Arl N., Nielsen, R.L., Pamukcu, A., Plank, T., Rasmussen, D.J., Roberge, J., Schiavi, F., Schwartz, Kei S., Shimizu, K., Shimizu, N., Thomas, J.B., Thompson, G.T., Tucker, J.M., Ustunisik, G., Waelkens, C., Zhang, Y., Zhou, T., 2021. Silicate melt inclusions in the new millennium: a review of recommended practices for preparation, analysis, and data presentation. Chemical Geology 120145.

Rowe, M.C., Kent, A.J., Nielsen, R.L., 2007. Determination of sulfur speciation and oxidation state of olivine hosted melt inclusions. Chem. Geol. 236, 303–322.

Schreiber, H.D., Merkel Jr., R.C., Schreiber, V.L., Balazs, G.B., 1987. Mutual interactions of redox couples via electron exchange in silicate melts: models for geochemical melt systems. Journal of Geophysical Research: Solid Earth 92, 9233–9245.

Sharp, T.G., Stevenson, R.J., Dingwell, D.B., 1996. Microlites and "nanolites" in rhyolitic glass: microstructural and chemical characterization. Bull. Volcanol. 57, 631–640.

Shorttle, O., Moussallam, Y., Hartley, M.E., Maclennan, J., Edmonds, M., Murton, B.J., 2015. Fe-XANES analyses of Reykjanes Ridge basalts: implications for oceanic crust's role in the solid Earth oxygen cycle. Earth Planet. Sci. Lett. 427, 272–285.

Sutton, S.R., Lanzirotti, A., Newville, M., Rivers, M.L., Eng, P., Lefticariu, L., 2017. Spatially resolved elemental analysis, spectroscopy and diffraction at the GSECARS Sector at the Advanced Photon Source. J. Environ. Qual. 46, 1158–1165.

Sutton, S.R., Lanzirotti, A., Newville, M., Dyar, M.D., Delaney, J., 2020. Oxybarometry and valence quantification based on microscale X-ray absorption fine structure (XAFS) spectroscopy of multivalent elements. Chem. Geol. 531, 119305.

Tassara, S., Reich, M., Cannatelli, C., Konecke, B.A., Kausel, D., Morata, D., Barra, F., Simon, A.C., Fiege, A., Morgado, E., 2020. Post-melting oxidation of highly primitive basalts from the southern Andes. Geochim. Cosmochim. Acta 273, 291–312.

Tuffen, H., Flude, S., Berlo, K., Wadsworth, F., Castro, J., 2021. Obsidian. In: Alderton, D., Elias, S.A. (Eds.), Encyclopedia of Geology, Second edition. Academic Press, Oxford, pp. 196–208.

Wallace, P.J., Carmichael, I.S.E., 1994. S speciation in submarine basaltic glasses as determined by measurements of SKα X-ray wavelength shifts. Am. Mineral. 79, 161–167.

Wallace, P.J., Anderson Jr., A.T., Davis, A.M., 1999. Gradients in H_2O, CO_2, and exsolved gas in a large-volume silicic magma system: Interpreting the record preserved in melt inclusions from the Bishop Tuff. Journal of Geophysical Research: Solid Earth 104, 20097–20122.

Wallace, P.J., Dufek, J., Anderson, A.T., Zhang, Y., 2003. Cooling rates of Plinian-fall and pyroclastic-flow deposits in the Bishop Tuff: inferences from water speciation in quartz-hosted glass inclusions. Bull. Volcanol. 65, 105–123.

Wallace, P.J., Plank, T., Bodnar, R.J., Gaetani, G.A., Shea, T., 2021. Olivine-hosted melt inclusions: a microscopic perspective on a complex magmatic world. Annual Review of Earth and Planetary Sciences 49.

Watkins, J.M., Gardner, J.E., Befus, K.S., 2017. Nonequilibrium degassing, regassing, and vapor fluxing in magmatic feeder systems. Geology 45, 183–186.

Waychunas, G.A., Apted, M.J., Brown, G.E., 1983. X-ray K-edge absorption spectra of Fe minerals and model compounds: near-edge structure. Phys Chem Minerals 10, 1–9.

Weaver, S.L., Wallace, P.J., Johnston, A.D., 2011. A comparative study of continental vs. intraoceanic arc mantle melting: experimentally determined phase relations of hydrous primitive melts. Earth Planet. Sci. Lett. 308, 97–106.

Wilke, M., Farges, F., Petit, P.-E., Brown Jr., G.E., Martin, F., 2001. Oxidation state and coordination of Fe in minerals: an Fe K-XANES spectroscopic study. Am. Mineral. 86, 714–730.

Wilke, M., Partzsch, G.M., Bernhardt, R., Lattard, D., 2004. Determination of the iron oxidation state in basaltic glasses using XANES at the K-edge. Chem. Geol. 213, 71–87.

Wilke, M., Schmidt, C., Farges, F., Malavergne, V., Gautron, L., Simionovici, A., Hahn, M., Petit, P.-E., 2006. Structural environment of iron in hydrous aluminosilicate glass and melt-evidence from X-ray absorption spectroscopy. Chem. Geol. 229, 144–161.

Wilke, M., Farges, F., Partzsch, G.M., Schmidt, C., Behrens, H., 2007. Speciation of Fe in silicate glasses and melts by in-situ XANES spectroscopy. Am. Mineral. 92, 44–56.

Wilke, M., Jugo, P.J., Klimm, K., Susini, J., Botcharnikov, R., Kohn, S.C., Janousch, M., 2008. The origin of S^{4+} detected in silicate glasses by XANES. Am. Mineral. 93, 235–240.

Wilke, M., Klimm, K., Kohn, S.C., 2011. Spectroscopic studies on sulfur speciation in synthetic and natural glasses. Rev. Mineral. Geochem. 73, 41–78.

Zhang, H.L., Hirschmann, M.M., Cottrell, E., Newville, M., Lanzirotti, A., 2016. Structural environment of iron and accurate determination of $Fe^{3+}/\Sigma Fe$ ratios in andesitic glasses by XANES and Mössbauer spectroscopy. Chem. Geol. 428, 48–58.

Zhang, H.L., Cottrell, E., Solheid, P.A., Kelley, K.A., Hirschmann, M.M., 2018. Determination of $Fe^{3+}/\Sigma Fe$ of XANES basaltic glass standards by Mössbauer spectroscopy and its application to the oxidation state of iron in MORB. Chem. Geol. 479, 166–175.